Fall 12-19-2019

ACOUSTIC DESIGN OPTIMIZATION WITH ISOGEOMETRIC ANALYSIS AND DIFFERENTIAL EVOLUTION

Garrett W. Dodgen
University of Texas at Tyler

ACOUSTIC DESIGN OPTIMIZATION WITH ISOGEOMETRIC ANALYSIS AND DIFFERENTIAL EVOLUTION

by

GARRETT WADE DODGEN

A thesis submitted in partial fulfillment
of the requirements for the degree of
Master of Science in Mechanical Engineering
Department of Mechanical Engineering

Tahsin Khajah, Ph.D., Committee Chair

College of Engineering

The University of Texas at Tyler
December 2019

The University of Texas at Tyler
Tyler, Texas

This is to certify that the Master's Thesis of

GARRETT WADE DODGEN

has been approved for the thesis requirement on
November 13, 2019
for the Master of Mechanical Engineering degree

Approvals:

Tahsin Khajah
Thesis Chair: Tahsin Khajah, Ph.D.

Shih-Feng Chou
Member: Shih-Feng Chou, Ph.D.

Chung Goh
Member: Chung Hyun Goh, Ph.D.

Nael Barakat
Chair, Department of Mechanical Engineering

Dean, College of Engineering

Table of Contents

List of Figures

List of Tables

Abstract

ACOUSTIC DESIGN OPTIMIZATION WITH ISOGEOMETRIC ANALYSIS AND DIFFERENTIAL EVOLUTION

Garrett Wade Dodgen

Thesis Chair: Tahsin Khajah, Ph.D.

The University of Texas at Tyler
December 2019

The objective of this study is to utilize shape optimization to enhance the performance of devices relying on acoustic wave propagation. Particularly, the shape of a horn speaker and an acoustic energy harvester were optimized to enhance their performance at targeted frequencies. High order Isogeometric Analysis (IGA) was performed to estimate the acoustic pressure with minimum geometry and pollution errors [1]. The analysis platform was then combined with Differential Evolution (DE) to optimize the geometry of the horn speaker and energy harvester at a given frequency. These cases effectively demonstrate two applications of Isogeomtric shape optimization for devices relying on acoustic wave propagation. The horn shape was previously optimized using conventional FEA [2]. The study performed to optimize the sound energy harvester demonstrates the effectiveness of isogeometric shape optimization for novel applications. It was shown that the proposed platform can generate tunable designs that reach their optimum performance at the desired frequencies. The back-reflection of the horn speaker was reduced considerably by optimizing the shape of the horn boundary. Tikhonov regularization was used to avoid finding wiggly solutions and ensure ease of manufacturing. The geometry of the energy harvester was optimized and tuned for a range of targeted frequencies by optimizing its defining parameters, its placement angle, and developing an

optimized variable channel width. The DE algorithm, which is known for finding the global minimum, successfully updated the design geometries and identified the global minimum in most cases studied in this thesis.

Chapter 1

Introduction

1.1 Background

Conventional Finite Element Analysis (FEA) is widely used for shape optimization. However, there is a disconnect between how an object is modeled with Computer Aided Design (CAD) software and FEA analysis. Currently, geometries in CAD are described using Non-Uniform Rational B-Splines (NURBS). However, in order to perform FEA, the geometry must be re-generated and re-meshed for each objective function evaluation. This process is not only time consuming, but also leads to loss of geometric details in the discretized model. To get accurate results for complex shapes, very fine meshing must be performed which greatly increases computational cost [3].

To bridge this gap between modeling and analysis, Isogeometric Analysis (IGA) was developed. This is a method of performing FEA using the NURBS to describe both geometry and solution space, allowing for accurate representation of shapes to be used rather than approximations. IGA has been shown to be a potentially better method of performing acoustic analysis through increased accuracy and lower computational costs. It was shown that the geometry and pollution error, which is phase shift error, is under control in high order IGA [4][5]. Furthermore, any change in geometry is automatically adopted in IGA facilitating the shape optimization.

These traits make acoustic analysis with IGA a promising alternative to conventional FEA for performing optimization. Due to the need for more efficient products and energy harvesting devices, this thesis performs optimizations of two acoustic devices

that demonstrate IGA and DE's application for acoustic product development. Problem Statement

In this study acoustic optimization was used to optimize two devices, an acoustic horn, and energy harvester. The back-reflection of the acoustic horn was minimized while the acoustic pressure of the energy harvester was optimized. In both of these cases the solution is not intuitive, in other words, the correlation between shape and acoustic field is not apparent. Also, in both cases studied many independent parameters were involved in defining the shape of each device. It was necessary to simultaneously find the optimum value of these parameters to find the best design possible. Hence it was necessary to adopt an optimization strategy that can control many independent variables and yet be fast enough to obtain the optimum results in a timely manner. Hence, Differential Evolution (DE) was chosen which was shown to possess both of the above-mentioned properties [6][7].

1.2 Outline of Thesis

This thesis is structured as follows: Chapter One provides an introduction to the problems covered in this study, including the background and motivation. Chapter Two briefly describes IGA, its background and formulation. Chapter Three discusses the fundamentals of DE. In Chapter Four, the acoustic horn problem is introduced by providing the problem description and its formulation, then describes the optimization methodology used. This chapter also discusses the results of the optimum solutions found for the acoustic horn. Chapter Five discusses the optimization of sound energy harvesting, describes how

it was optimized, and presents a study on the performance of the optimum solutions found. The results of this study are summarized and discussed in Chapter Six.

Chapter 2

Isogeometric Analysis

2.1 B-Splines

B-spline basis function of degree p (order p +1) is the Cox-de Boor recursion formula [8]:

$$N_{i,0}(\xi) = \begin{cases} 1, & \text{if } \xi_i \leq \xi < \xi_{i+1}, \\ 0, & otherwise \end{cases} \tag{1}$$

$$N_{i,p}(\eta) = \frac{\xi - \xi_i}{\xi_{i+p} - \xi_i} N_{i,p-1}(\xi) + \frac{\xi_{i+p+1} - \xi}{\xi_{i+p+1} - \xi_{i+1}} N_{i+1,p-1}(\xi) \tag{2}$$

where p is the polynomial order and n is the number of basis functions. Any singularity of 0/0 is defined as zero and u_i is a knot, and the knot vector $\Xi = \{\xi_0,\ldots,\xi_m\}$ comprised of a non-decreasing series of real numbers. If knots are equally spaced in Ξ, then it is considered uniform, otherwise it is nonuniform.

A first-order B-spline basis function is identical to its Lagrangian counterpart used in FEA. The B-spline basis function's first derivative is calculated with the following:

$$\frac{d}{d\xi} N_{i,p}(\xi) = \frac{p}{\xi_{i+p} - \xi_i} N_{i,p-1}(\xi) - \frac{p}{\xi_{i+p+1} - \xi_{i+1}} N_{i+1,p-1}(\xi) \tag{3}$$

The number of required shape functions for both B-splines and the FEA Lagrangian are similar. The B-spline curves are then constructed as a linear combination of B-spline basis functions:

$$\mathbf{C}(\xi) = \sum_{i=1}^{n} N_{i,p}(\xi)\mathbf{B}_i \tag{4}$$

This is expanded into the B-spline surface:

$$\mathbf{S}(\xi,\eta) = \sum_{i=1}^{n}\sum_{j=1}^{m} N_{i,p}(\xi)M_{j,q}(\eta)\mathbf{B}_{i,j} \tag{5}$$

With $B_{i,j}, i = 1,2,...,n, j = 1,2,...,m$ are control points, $N_{i,p}(\xi)$ and $M_{j,q}(\eta)$ are the univariate B-spline functions of order p and q relating to the knot vectors $\Xi_1 = \{\xi_1,\xi_2,...,\xi_{n+p+1}\}$ and $\Xi_2 = \{\eta_1,\eta_2,...,\eta_{m+q+1}\}$ respectively.

2.2 NURBS Overview

NURBS is a mathematical model for producing smooth and accurate representations of geometries [9]. Using NURBS, accurate representations of both polynomials and conic sections such as circles, spheres and ellipsoids can be generated. NURBS have the advantage of assigning each control point a weight that can help to refine the shape. If the weights of each control point are equal, NURBS basis functions reduce to B-splines. Thus, B-splines are a subset of NURBS.

2.3 NURBS Definition

Assume $a = 0$, $b = 1$, and the weights $w_i > 0$ for all i, the NURBS shape functions are defined:

$$R(\xi) = \frac{N_{i,p}(\xi)w_i}{\sum_{i=1}^{n} N_{i,p}(\xi)w_i} \tag{6}$$

The general definition of a NURBS curve:

$$\mathbf{C}(\xi) = \sum_{i=1}^{n} R_{i,p}(\xi)\mathbf{P}_i \tag{7}$$

and the expansion to NURBS surfaces being defined as:

$$\mathbf{S}(\xi,\eta) = \sum_{i=1}^{n}\sum_{j=1}^{m} R_{i,j}^{p,q}(\xi,\eta)\mathbf{P}_{i,j} \tag{8}$$

and where basis functions:

$$R_{i,j}^{p,q}(\xi,\eta) = \frac{N_{i,p}(\xi)M_{j,q}(\eta)w_{i,j}}{\sum_{i=1}^{n}\sum_{j=1}^{m} N_{i,p}(\xi)M_{j,q}(\eta)w_{i,j}} \tag{9}$$

Similarly one can define the NURBS volume using tensor products [8]. However the scope of this study does not require volumetric NURBS patches so their definitions are omitted.

2.4 Isogeometric Analysis

IGA is a method of performing FEA using NURBS as the basis functions for analysis [10]. Using NURBS instead of conventional discretized boundaries of FEA

provides the benefit of more accurately representing the true geometry of the boundary using exact curves rather than polynomial approximations, thus potentially yielding more accurate simulation results. Many CAD software use NURBS to represent their generated model, and IGA can help improve the relationship between design and analysis.

Conventional FEA utilizes Lagrange polynomials as basis functions, thus in FEA software, a CAD model must be discretized into a mesh. This meshing process is very time consuming and can only approximate the original shape as defined by the CAD program. Potential issues that arise during this process are loss of detail and small imperfections in the original geometry being lost due to shape approximation, depending on the parameters of the meshing process. These issues can be reduced by increasing the mesh density or employing higher order meshes but this increases the computational cost without eliminating the error.

IGA uses NURBS as the basis functions for performing FEA, preserving the accurate geometry and reducing the computational time needed for remeshing.

From the previous NURBS formulation, the geometry on an IGA element:

$$x^e(\tilde{\xi}) = \sum_{a=1}^{n_{en}} \mathbf{P}_a^e R_a^e(\tilde{\xi}) \tag{10}$$

with $n_{en} = (p + 1)^{d_p}$ and d_p being the spatial dimension. Similarly, the field $u(x)$ is defined:

$$\mathbf{u}(\tilde{\xi}) = \sum_{a=1}^{n_{en}} \mathbf{d}_a^e R_a^e(\tilde{\xi}) \tag{11}$$

$\mathrm{d}_a^e R_a^e$ is a set of control variables. Due to the parametric definition of IGA basis functions, two mapping for integration must be considered:

$$\int_{\Omega} f(x)d\Omega = \sum_{e=1}^{n_{el}} \int_{\Omega^e} f(x)d\Omega = \sum_{e=1}^{n_{el}} \int_{\hat{\Omega}}^{e} f(x(\Xi))|J_{\Xi}|d\hat{\Omega} \\ = \sum_{e=1}^{n_{el}} \int_{\bar{\Omega}}^{e} f(x(\bar{\phi}^e(\bar{\Xi})))|J_{\Xi}||J_{\bar{\Xi}}|d\bar{\Omega} \tag{12}$$

$\bar{\Omega}$ and $\hat{\Omega}$ are representing the parent and parameter spaces. Also, Ω is representing the physical space.

The performance of IGA was compared with conventional FEM [3]. This study performed the structural analysis of an Aortic valve in both methods. To achieve similar results, the IGA model needed a little over 1 hour of computational time, while the FEA model had an analysis time of 550 hours, a 99.7% reduction in computational time.

This is due to the more complex meshing process required to perform FEA. The number of nodes required to perform the study accurately in FEA was 153646 nodes. IGA was able to achieve the same results with only 762 nodes. For this particular model, that is a 95.5% decrease in the number of nodes.

These results highlight why IGA is preferable for optimization problems, the drastic reduction in computational cost allows for more complex and thorough optimization studies to be run without being time prohibitive or achieve similar accuracy with smaller computational cost for a given accuracy.

Presently, many studies have coupled IGA with optimization. This combination has been used many times for structural optimization, such as for windmill blades [11], support structures [12], and structural shells [13].

Chapter 3

Differential Evolution

The optimizations performed in this study use Differential Evolution (DE). This method is an iterative evolutionary method that generates a mutated population vector, calculates the objective function value by performing analysis, and compares the result value with the initial value or lowest value thus obtained [5]. If the result is improved, it becomes the new basis for the next mutated population. Doing so optimizes by continually checking over an increasingly narrow mutation range to find an optimal solution. In the case of this horn optimization, a population vector of size NP, ($10 * ($*Number of Mutable Control Points*$)$), is used. For each generation (G), a population vector is generated as:

$$x_{i,G}, i = 1,2,...,NP \tag{13}$$

The mutation vector for each G is generated as follows:

$$v_{i,G+1} = x_{r1,G} + F \cdot (x_{r2,G} - x_{r3,G}) \tag{14}$$

using random indexes $r_1, r_2, r_3 \in 1,2,...,NP$, which are mutually different, integer and $F > 0$. Integers r_1, r_2, and r_3 are randomly chosen and are different from running index i, so NP must be greater than or equal to four, allowing for this condition.

The real and constant factor F controls amplification of the differential variation ($x_{r2,G} - x_{r3,G}$) and is in the range of 0 to 2. Crossover is introduced to increase the variety of the mutated parameter vectors. The trial vector:

$$u_{i,G+1} = (u_{1i,G+1}, u_{2i,G+1}, \ldots, u_{Di,G+1}) \tag{15}$$

is generated using:

$$u_{ji,G+1} = \begin{cases} v_{ji,G+1}, & \text{if } (randb(j) \leq CR \text{ or } j = rnbr(i)) \\ x_{ji,G}, & \text{if } (randb(j) \geq CR \text{ or } j \neq rnbr(i)) \end{cases} \quad j = 1, 2, \ldots, D. \tag{16}$$

where, $randb(j_{DE})$ is the jth evaluation of a uniform random number generator with outcome $\in$ [0,1]. CR is a crossover constant determined by the user, and $rnbr(i)$ is a randomly chosen index $\in$ 1,2,...,D, that ensures that $u_{i,G+1}$ gets a parameter from $v_{i,G+1}$.

Hence, DE is an algorithm that generates a population of defined variables, with each member of the population being mutated from a previous population. For each set of mutated variables, the problem is analyzed and the member group that achieves the best result becomes the basis for the next population set. This process continues for predefined population size and number of iterations. One of DE's primary advantages is its ability to simply handle a high number of unrelated variables. Multiple variables can be optimized simultaneously without needing extra formulation to directly link them together. Additionally, DE is a good choice for problems that have many local optima but only one global optimum [6]. The randomness of the initial population pool and subsequent mutations allow the algorithm to diversify the search and reduce the dependency on the initial guess.

The performance of DE in solving a few benchmark problems was compared with other commonly used evolutionary methods. Where DE outperformed other evolutionary methods by a large margin. For example, it took DE only 260 generations to solve one of the simplest benchmark problems. While the next best performing algorithm, a Parallel Genetic Algorithm (PGA), required 1170 generations [6]. When dealing with a more complicated optimization problem, the Foxholes Function, a problem with many drastic local optima, DE was still the best performing method but only slightly more so than PGA, with DE taking 1200 generations and PGA 1256 generations.

Chapter 4

Acoustic Horn Optimization

4.1 Problem Overview

While computational cost of IGA and FEM are comparable for equal number of degrees of freedom, IGA yields higher accuracy. In other words, for a given accuracy the computational cost can be considerably reduced. To find the optimum solution it is necessary to evaluate the objective function many times by performing analysis. Hence, reducing the computational cost for a single evaluation of the objective function reduces the optimization time considerably. An isogeometric horn shape optimization was considered in this study. The horn shape considered was similar to a horn to those found in commercial speakers and musical instruments, such as a bugle or trumpet. A common problem in horn speakers is back-reflection. In which a portion of the outgoing wave reflects back into the wave source due to interactions with the shape of the wave-guide and its pressure. This can distort the outgoing wave, as the total wave becomes the interaction of two separate waves rather than a single wave. Thus, the objective of the optimization is to minimize the back-reflection by changing the horn shape.

This problem has been investigated using conventional FEA and both gradient-based and evolutionary optimization [11][12].

4.2 Problem Formulation

Consider the 2D simple horn geometry shown in Fig.1, which is similar to the one studied in [2] and previously studied in [14][15]. A linear plane waves enters the domain, Ω, from the inlet boundary, Γ_{in}. Domain *Omega* is assumed to have uniform properties filled with air. The speed of sound within this medium is assumed to be $c = 343 m/s$.

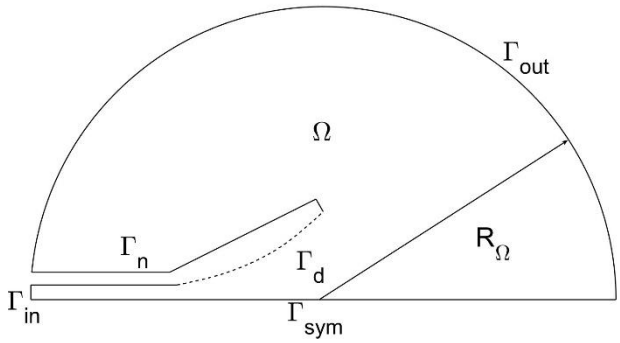

Figure 1: Boundaries and Domain of Horn Mesh

A first order Engquis-Majda [16] absorbing boundary condition is applied at the fictitious boundary Γ_{out} to artificially truncate the computational domain mimicking the propagation of the outgoing wave into the farfield. This boundary simulates the effect of an infinite domain for the wave to propagate out. Boundaries denoted by Γ_n are considered to be sound-hard or rigid. While in a real-world setup no material can be true sound-hard, it is assumed that horn is composed of a material such as aluminum that makes any potential effects of this negligible.

Across Γ_{sym}, the horn model is mirrored, therefore only the upper half was considered in analysis since all results will be symmetric. The boundary representing the horn is denoted by $\Gamma_{d,}$ which is the boundary to be modified to maximize the impedance

matching and reduce back-reflection. Γ_d is also a sound-hard boundary similar to Γ_n. It is assumed that the horn speaker is wide enough that its finite extension in the cross-planar direction has no effect on its performance.

The infinite space is artificially truncated with a semi-circle and an Engquis-Majda boundary condition is imposed on this artificial boundary, Γ_{out}. The governing equation for sound propagation is the linear wave equation for acoustic pressure P, in a domain comprised of a loss-less adiabatic medium, and where *c* denotes the speed of sound and Δ is the Laplacian operator, the following mathematical model is used [13]:

$$\frac{\partial^2 P}{\partial t^2} = c^2 \Delta P \tag{17}$$

In a case with a planar channel, *waveguide*, with infinite extension in the 3rd dimension and single-frequency planar waves in the waveguide can be expressed with,

$$P(x,t) = Ae^{i(kx\cdot n+\omega t)} + Be^{i(kx\cdot n+\omega t)}, \quad A, B \in \mathbb{C} \tag{18}$$

where ω is the angular frequency of the wave, and $k = \omega/c$ is the wave number. The first term of Eq.(18) is for the incident wave and the second term is the reflected wave. At the inlet, differentiating Eq.(18) yields:

$$\frac{\partial P}{\partial t} = Ai\omega e^{i(kx\cdot n+\omega t)} + Bi\omega e^{i(kx\cdot n+\omega t)} \tag{19}$$

$$\frac{\partial P}{\partial n} = Aike^{i(kx\cdot n+\omega t)} + Bike^{i(kx\cdot n+\omega t)} \tag{20}$$

Where $\partial P/\partial n$ is the derivative in the outward normal direction. Using Eq.(19) and Eq.(20), along with $kc = \omega$ one can obtain:

$$\frac{\partial P}{\partial t} + c\frac{\partial P}{\partial t} = 2i\omega A e^{i(kx\cdot n+\omega t)} \tag{21}$$

For a wave of type (18), the amplitude A of the incident wave is set independent of the B, the amplitude of the reflected wave. An Engquist boundary condition is applied to the exiting boundaries of the mesh to eliminate reflection of waves propagating in the normal direction on the Γ_{out} boundaries [16],

$$\frac{\partial P}{\partial t} + c\frac{\partial P}{\partial n} + \frac{c}{2R_\Omega}P = 0 \tag{22}$$

The other boundaries, Γ_n, are a sound hard case. On Γ_{sym} the following conditions are applied to this symmetry plane:

$$\frac{\partial P}{\partial n} = 0 \quad \text{on } \Gamma_n \cup \Gamma_{sym} \tag{23}$$

Applying to Eq.(17) the boundary conditions (21)-(23) and the ansatz $P(x,t) = p(x)e^{i\omega t}$ for time harmonic, single-frequency solutions, the following *Helmholtz equation* for the complex amplitude function p is obtained:

$$i\omega p + c\frac{\partial p}{\partial n} = 2i\omega A \quad \text{on } \Gamma_{in} \tag{24a}$$

$$\frac{\partial P}{\partial n} = 0 \quad \text{on } \Gamma_n \cup \Gamma_{sym} \tag{24b}$$

$$c^2\Delta p + \omega^2 p = 0 \quad \text{in } \Omega \tag{24c}$$

$$(i\omega + \frac{c}{2R_\Omega})p + c\frac{\partial p}{\partial n} = 0 \quad \text{on } \Gamma_{out} \tag{24d}$$

Then the pressure *p* can be approximated as:

$$p_h(x) = \sum_{j \in K} p_J w_J(x), \quad p_J \in \mathbb{C} \tag{25}$$

where:

$$w_J(x_K) = \begin{cases} 1, & \text{if } k = J, \\ 0, & \text{if } k \neq J \end{cases}$$

as the solution of the following weak form:

$$\begin{aligned} c^2 \int_{\Omega_h} \nabla w_j \cdot \nabla p_h d\Omega - \omega^2 \int_{\Omega_h} w_j p_h d\Omega + i\omega c \int_{\Gamma_{in} \cup \Gamma_{out}} w_j p_h d\Gamma \\ + \frac{c^2}{2R_\Omega} \int_{\Gamma_{out}} w_j p_h d\Gamma = 2i\omega c A \int_{\Gamma_{in}} w_j d\Gamma \quad \forall j \in K \end{aligned} \tag{26}$$

The objective of the optimization is to modify the shape of the horn ”bell” to improve the efficiency of the speaker. This is achieved by minimizing the objective function *J*, which is the square of the magnitude of the reflected wave integrated over the inflow boundary:

$$J = \frac{1}{2} \int_{\Gamma_{in}} |p_h - A|^2 d\Gamma \tag{28}$$

4.3 Shape Modification

The objective function's value depends of the shape of the horn bell, Γ_d. The initial shape, Γ^{ref}_d is chosen to be curve defined by:

$$y_{ref}(x) = 0.0081e^{3.6184x} \qquad 0.5 < x < 1.0 \tag{29a}$$

$$y_{ref}(0.5) = 0.05 \tag{29b}$$

$$y_{ref}(1.0) = 0.3 \tag{29c}$$

This curved initial shape is to prime the optimization by starting from a curve which already closely resembles typical horn shapes as shown in Fig.2. During optimization, the endpoints of the curve are locked to preserve mesh connectivity. The curve is modified by obtaining a vector, α, that indicates a value to move the point along the normal of a straight-line curve connecting the two endpoints of Γ^{ref}_d as demonstrated in Fig. 3:

$$x_{ref} = x_{ref} + \alpha(x_{ref})n_{x,ref} \tag{30a}$$

$$y_{ref} = y_{ref} + \alpha(y_{ref})n_{y,ref} \tag{30b}$$

$$n_{x,ref} = -0.44723, \quad n_{y,ref} = 0.89445 \tag{30c}$$

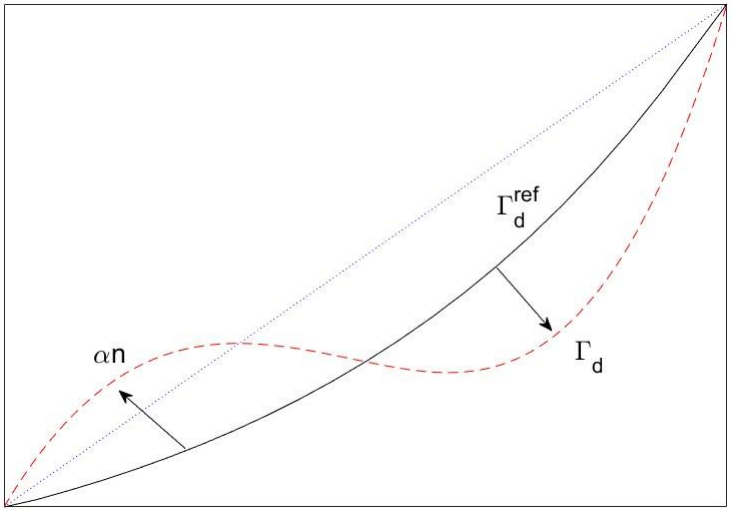

Figure 2: Modification of the design boundary

The vector α moves the control points of the NURBS curve of Γ_{ref}. The NURBS curve is then created from this set of updated control points.

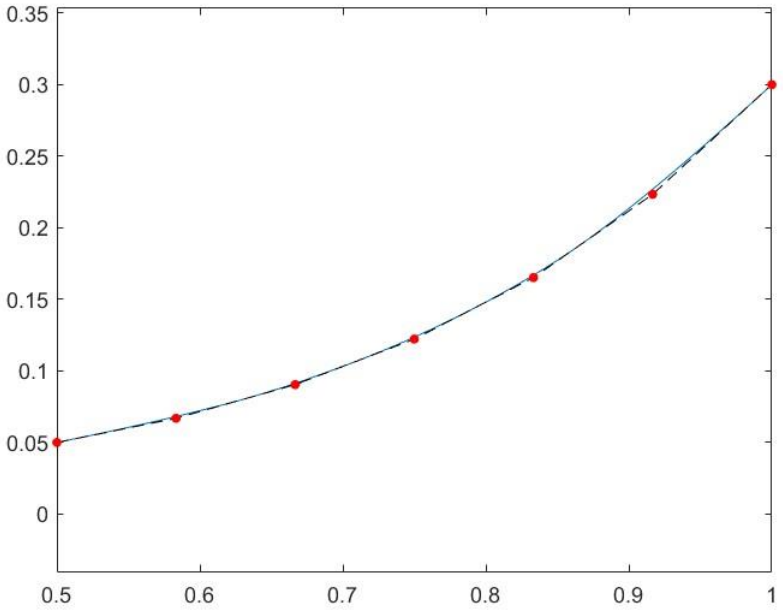

Figure 3: Initial NURBS curve of Γ_{ref}

For an example of how the horn bell's shape is modified by vector α, $\alpha = [-0.06, 0.02, 0.00, -0.10, 0.06]$ was considered which modified the horn shape as depicted in Fig. 4. This shows that while the control points determine the shape of the curve. This method allows for the entire curve to be modified only using five parameters, which reduces the computation cost even more when compared with FEA.

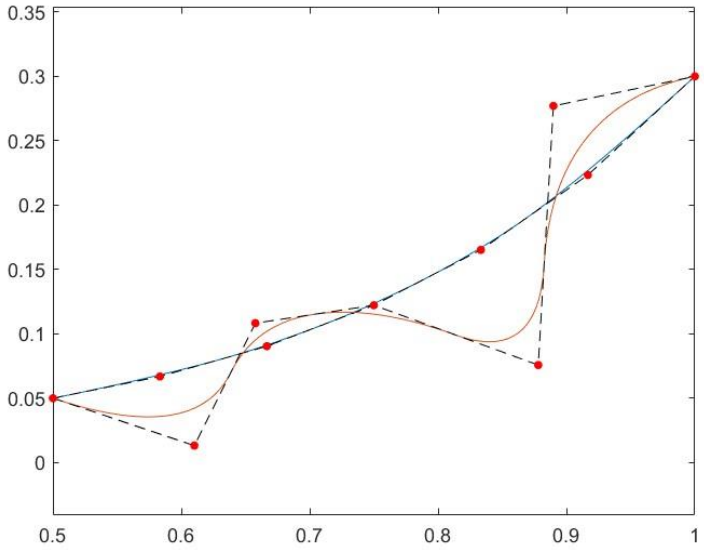

Figure 4: Example of Γ_d

One important factor to consider during any problem with mesh modification is to ensure that mesh integrity remains intact, otherwise the results may not be reliable. A study analyzing this horn problem using conventional FEA had a few issues with the mesh being deformed and having mesh overlap [2]. For the NURBS generated horn mesh, the control points movement were limited to set ranges that prevent overlap. However, during initial trials, a potential source of mesh failure was discovered.

The initial setup of the horn NURBS mesh is shown in Fig.5.

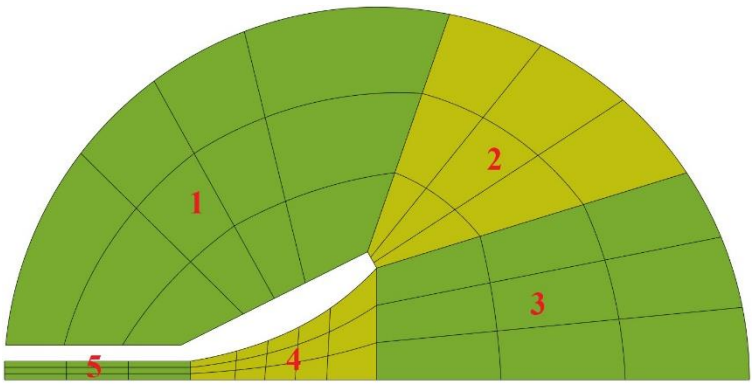

Figure 5: NURBS Multi-patch Surface of Horn

Each separately colored region is a NURBS Coons surface patch. A Coons surface is a surface generated by interpolating the space between four defined edges. The surface that will change throughout the optimization is Patch 4. This is a Coons patch defined by the Horn Design boundary Γ_d, a segment of the boundary of symmetry Γ_{sym}, the shared boundary with Patch 3, and the shared boundary with Patch 5. As the control points of Γ_d are moved described by Eq.30a - 30c, it was found that certain values of movement result in meshing issues, particularly when there is a large difference between the movement of neighboring control points.

To resolve this issue, the mesh was modified so that all the boundaries of Patch 4 were oriented so that all points with the mesh moved normal with Γ_d. The new NURBS multi-patch can be seen in Fig.6.

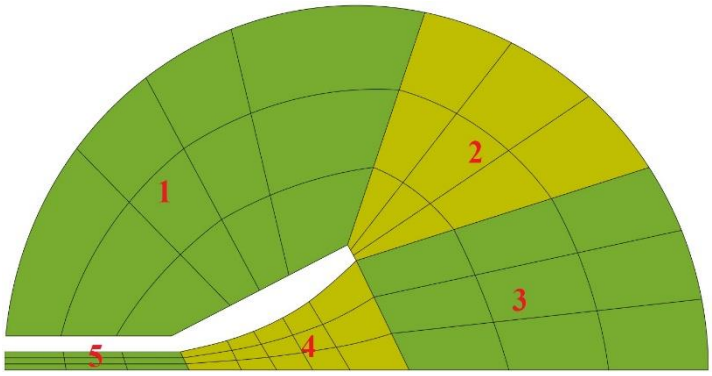

Figure 6: New NURBS Mesh

4.4 Model Verification

The IGA code was verified by comparing numerical and exact solution for a circular cylinder [3][17]. Consider a sound-hard circular cylinder problem of the 2D geometry as shown in Fig.7 where:

- Ω_d- Annulus domain of the problem
- R_0- Radius of sound-hard cylinder
- R_1- Radius of outer absorbing boundary
- C_0- Boundary of cylinder
- C_1- Boundary of outer absorbing boundary

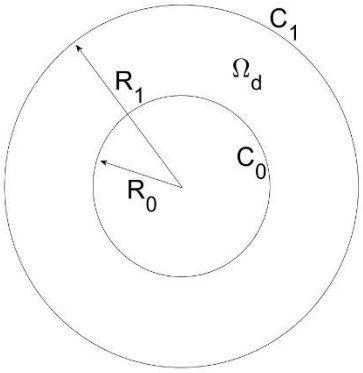

Figure 7: Verification Model Geometry

With an incident plane wave $u^{inc}(x) = e^{ikd\cdot x}$, d being the incidence direction. The exact soluiton for circular hard-obstacle is given by:

$$u_{sc}(r,\theta) = -\sum_{n=0}^{\infty} \epsilon_n i^n \frac{J_n(kr_0)}{H_n^{(1)}(kr_0)} H_n^{(1)}(kr)\cos n\theta \tag{31}$$

With Farfield-Pattern (FFP)

$$P(\theta) = -\left(\frac{2}{k\pi}\right)^{1/2} e^{-i\pi/4} \sum_{n=0}^{\infty} \epsilon_n \frac{J_n'(kr_0)}{H_n'^{(1)}(kr_0)} \cos n\theta \tag{32}$$

To obtain the derivatives, use the following recurrence formulas:

$$c_n'(z) = \frac{nc_n(z)}{z} - c_{n+1}(z) \qquad \text{and} \qquad c_n'(z) = -\frac{nc_n(z)}{z} + c_{n-1}(z) \tag{33}$$

Therefore,

$$\frac{d}{dr}H_0(kr) = H_0'(kr)k = -kH_1(kr) \qquad \text{and} \qquad \frac{d}{dr}H_1(kr) = H_0(kr) - \frac{H_1(kr)}{r} \tag{34}$$

Analogously,

$$\frac{d}{dr}J_0(kr) = -kJ_1(kr) \qquad \text{and} \qquad \frac{d}{dr}J_1(kr) = J_0(kr) - \frac{J_1(kr)}{r} \tag{35}$$

In general, $n = 1, 2, \ldots$

$$\frac{d}{dr}H_n(kr) = \frac{-nH_n(kr)}{r} + kH_{n-1}(kr) \tag{36}$$

$$\frac{d}{dr}J_n(kr) = \frac{-nJ_n(kr)}{r} + kJ_{n-1}(kr) \tag{37}$$

The following absolute error plot for the scatter field was produced using the same spline order p as in the horn model and the difference in results between the IGA analysis and exact solution is plotted in Fig.8:

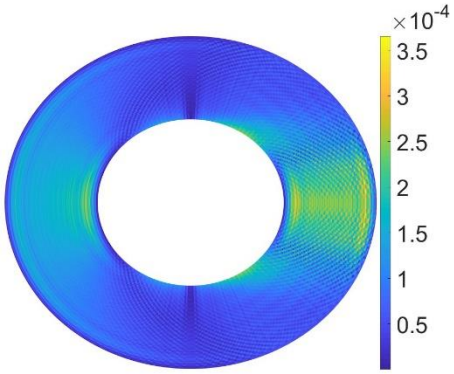

Figure 8: Verification Model Error Plot

The low errors present in the verification model indicate that the methodology analyzing the horn case is valid and the results obtained are reliable for the purpose of shape optimization.

4.5 Smoothing

More than one optimum solution can be found for each frequency. Smooth and regularized solutions are preferred to impose less manufacturing constrains. In order to regularize the solution Tikhonov regularization was used in this study.

Tikhonov regularization is a method to deal with ill-posed problems, especially when there is more than one possible solution. To achieve a smooth boundary, a new variable η is introduced such that:

$$-\alpha'' = \eta \qquad \text{on } \Gamma_d^{ref}$$

$$\alpha = 0 \qquad \text{at the end points of } \Gamma_d^{ref} \tag{38}$$

The Tikhonov regularized objective function now becomes:

$$j^{\epsilon}(\eta) = \frac{\epsilon}{2}\int_{\Gamma_d^{ref}} \eta^2 d\Gamma + \frac{1}{2}\int_{\Gamma_{in}} |p(\eta) - A|^2 d\Gamma \tag{39}$$

This application of Tikhonov regularization uses the sum of curvature of the bell curve to create the smoothing variable, η, thus with a higher curvature of the design, the objective value will also increase [18]. Also, ϵ is a constant to control the extent of the correspond objective function penalization.

It was shown that smoothing this algorithm can effectively avoid wiggly shapes as shown in Fig. 9 the optimum solution without smoothing is compared to the one obtained with smoothing. Both solutions are equally effective in reducing the back-reflection but the optimum solution found using smoothing is considerably simpler and imposes far less manufacturing constraints.

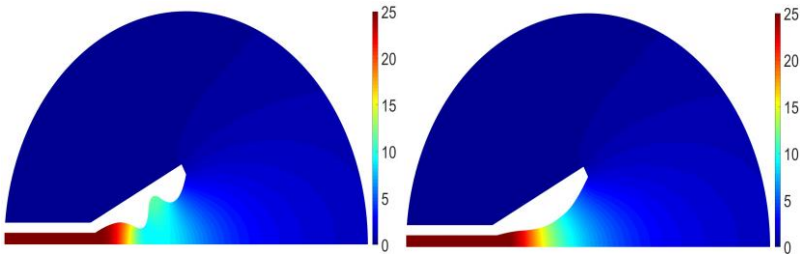

Figure 9: Comparison of the optimum solution found without (left) and with smoothing (right) at 500 Hz

As seen in Fig. 9, two similarly performing horns can have significantly different shapes, by while the two may have equal base values of *J*, the Tikhonov regularization increases the total objective function value by using the amount of curvature present on the shape. Thus if two equally performing horns with different shapes are analyzed, the one with less curvature will be more optimum.

4.6 Optimization Setup and Control Values

The horn shape optimization steps are outlined in the flowchart depicted in the Fig.10. The mesh was modified by a set of optimization design variables which were used to automatically update the IGA mesh. Then analysis was performed, and the objective function values were estimated. The value of the objective function is then compared with that of previous iterations and a new population was generated for the next iteration. When applying the Tikhonov smoothing, the population generated by DE algorithm was not used directly to update the horn boundary. Instead a new set of design variables, η was used along with the modified objective function presented in Eq.32 to obtain smooth solutions.

From a range of 300 Hz to 700 Hz in steps of 100 Hz, the initial mesh was analyzed to find J. These results are listed in Table 1. From these values it is indicated that the proposed initial horn shape performs best at 700Hz, since the value of the objective function J is minimum at this frequency.

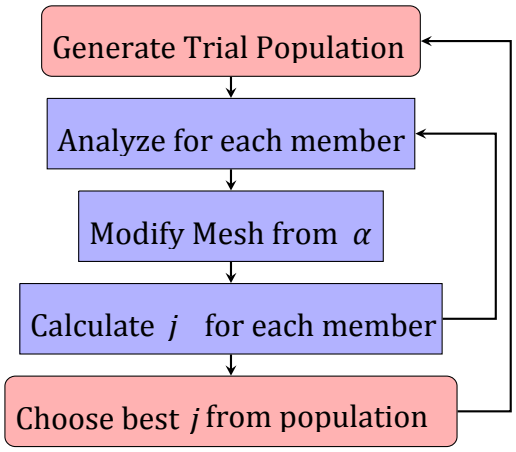

Figure 10: Optimization Flowchart

Table 1: Initial Horn *J* Values

Frequency (Hz)	*J*
300	0.0409
400	0.0039
500	0.0073
600	0.0080
700	0.0009

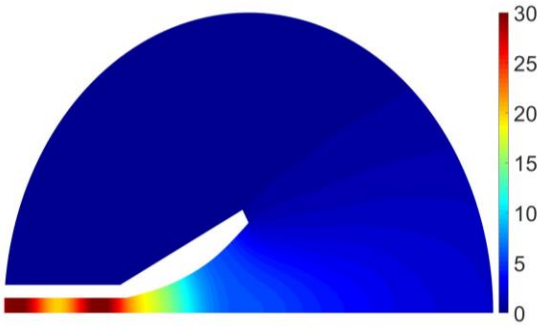

Figure 11: The square of the absolute value of the scattered field at 500Hz before optimization

The ”banding” or the alternating colors within the waveguide can be seen in Fig.11, which is a visual indication that there is significant back reflection into the waveguide. An optimized horn should minimize this banding and instead present a gradient, decreasing away from the source. It is evident from Fig.12 that back-reflection is reduced by shape optimization of the horn boundary.

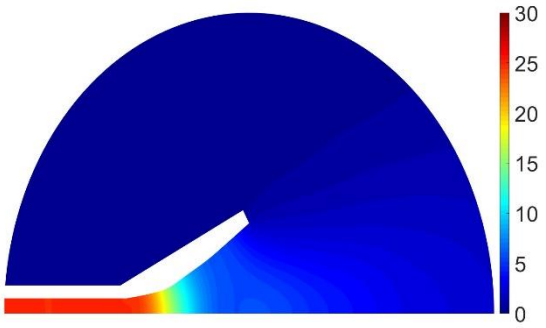

Figure 12: The square of the absolute value of the scattered field at 500Hz after optimization

The result shown Fig.12 also demonstrates how very subtle changes to the shape can have significant effects on the performance of the horn speaker. The difference between the shapes of the horn boundary before and after optimization shown in Fig.11 and Fig.12 respectively is not significant and difficult to visually notice. In this example 5 control points defining the horn shape were used as optimization design variables. Each optimization trial was run for 50 iterations with a population of 50.

4.7 Single Frequency Optimization

4.7.1 Without Smoothing

Shape optimization was performed to find the optimum shape of the horn boundary at frequencies of 300, 400, 500, 600, and 700Hz without smoothing. The values of the objective function for the optimized solutions and the corresponding frequencies are tabulated in Table 2.

Table 2: Single-frequency optimized horn objective function *J* Values (no smoothing)

Frequency (Hz)	300	400	500	600	700
J	2.361e-06	4.345e-07	1.329e-07	7.890e-07	3.849e-06

Each optimization run for the single frequencies without smoothing generated interesting but complex shapes, as shown in Fig. 13.

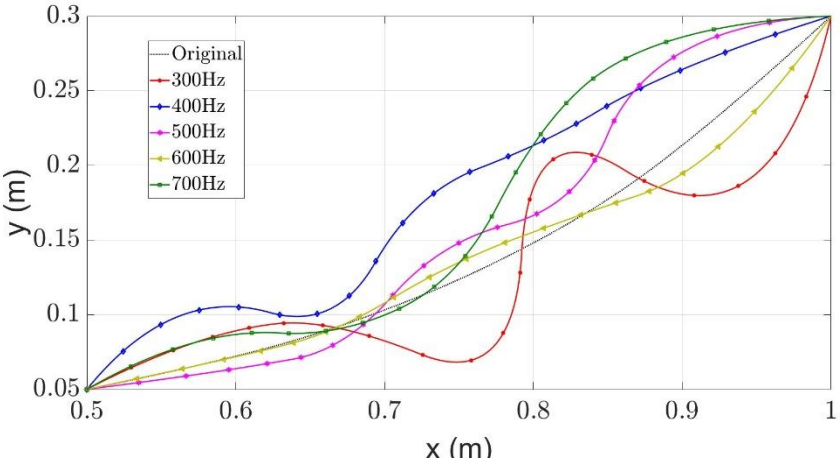

Figure 13: Comparison of Single-Frequency Optimized Horn Bells without smoothing

Most of the horn shapes exhibit a high degree of curvature, particularly in the case of the 300Hz optimization where at around 0.8m it almost has a vertical slope. Figure 14 compares the performance of each shape across the 300 to 700Hz frequencies, at steps of 20Hz.

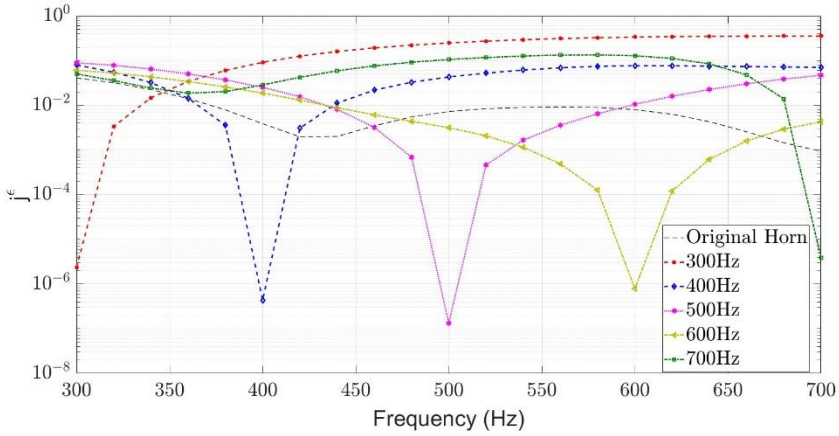

Figure 14: Comparison of Single-Frequency Optimized *J* values without smoothing

The effectiveness of single frequency optimization is evident in Fig. 14, the objective function value *J* reduced from about 10^{-3} to 10^{-6}. This is a significant decrease in the back reflection into the waveguide.

However, the results also demonstrate a potential negative effect of single-frequency optimization. While at the targeted frequencies, significant improvement was made, the optimized horn shapes often performed worse than the original horn shape for the rest of the frequency range. This would indicate that these shapes are less than ideal for an application that could potentially use a range of frequencies.

It is also interesting to note is that across the frequency range, the original horn exhibited two ”dips” in the back reflection. At around 420Hz and 700Hz, the original horn had a reduced objective function value *J* compared to the rest of the spectrum. The optimized shapes only demonstrated a single, large reduction, with the exception of the 700Hz optimization, which had a second, very minor decrease at 360Hz.

For these optimizations, the behavior of the DE iterations is shown in Fig.15.

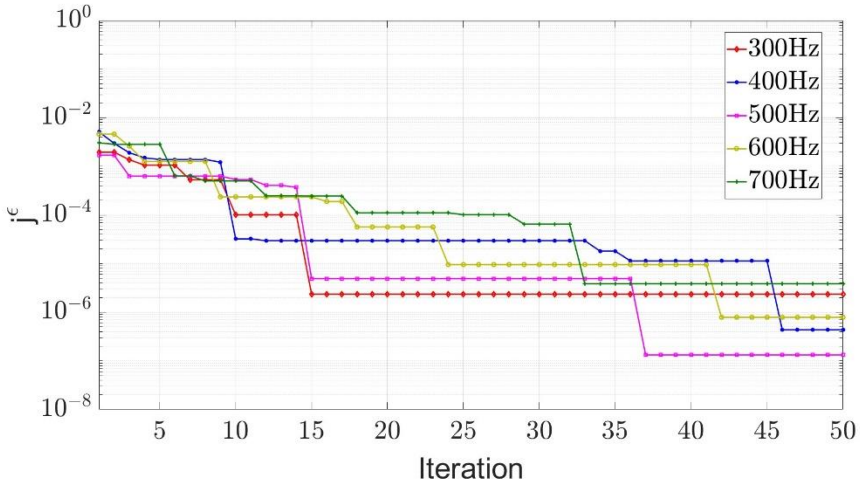

Figure 15: DE Behavior of Single Frequency Optimization without Smoothing

For about the first ten iterations, the optimization behavior was similar for each of the frequency cases. However after ten iterations, the objective function remained unchanged for many iterations which is seen as a 'plateau'. In some cases a sudden significant improvements were observed but then it would plateau again. This plateau behavior indicates that increasing the number of iterations may yield even better optimization. However, increasing the iterations also raises the computational time of optimization. At the 300Hz reached its minimum value at the 15th iteration.

During the first 25 iterations, the objective function was at most reduced from 10^{-2} to 10^{-4}, with all cases also reaching a plateau as well. A decrease from a starting value of $10^{-}2$ to 10^{-4} is a 99% reduction from the original value, however reduction to 10^{-6} is only enhancing the design further by 0.01% reduction from the starting value. The smallest reduction was the 700 Hz optimization, which achieved a 99.6% decrease in in back-reflection.

4.7.2 With Smoothing

Additionally, the single-frequency optimizations were run with smoothing. Table 3 list the objective function (J) values with smoothing.

Table 3: Single-frequency optimized horn objective function J Values (with smoothing)

Frequency (Hz)	300	400	500	600	700
J	9.049e-05	1.245e-05	6.598e-05	3.725e-04	1.051e-04

With smoothing, the objective function values were not reduced to those obtained without smoothing. In most cases, the objective function was decreased to 10^{-5}. However, the optimized boundaries are much easier to manufacture. These results demonstrate that in this case, the Tikonov regularization had a significant effect on the optimization. Figure 16 presents the smoothed optimized shapes for the 300-700Hz range frequencies.

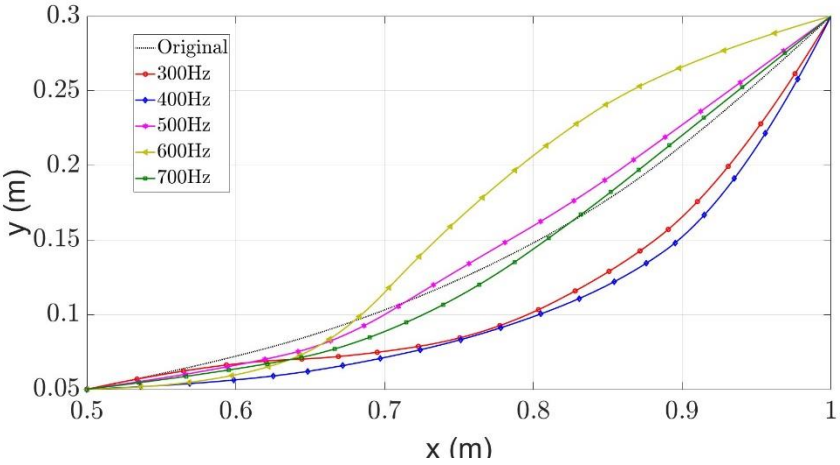

Figure 16: Comparison of Single-Frequency Optimized Horn Bells with smoothing

The smoothing effect can clearly be seen when comparing Fig.13 to Fig.16. The smoothed shapes exhibit much less curvature. There are also quite a few that closely match the base horn, with a few minor variations. The main outlier is the optimum boundary found for 600Hz shape optimization, which has a large concave section whereas all of the others are convex. The shape found for 300 and 400Hz are very similar but much more convex than any of the other shapes.

While the smoothing tended to produce higher values of objective function *J*, the corresponding optimum shapes showed improved global performance across the range of frequencies, as shown in Fig. 17.

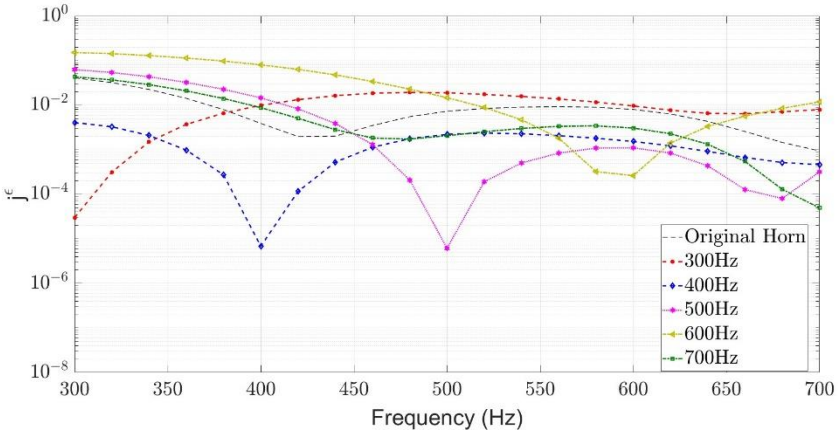

Figure 17: Comparison of Single-Frequency Optimized *J* values with smoothing

This is an interesting property that emerges despite there being no set optimization criteria to promote this behavior. This may be an emergent property of the smoothed shapes indicating that a smooth shape will be ideal for an optimization across a range of frequencies.

For these optimizations, the behavior of the DE iterations is shown in Fig.18.

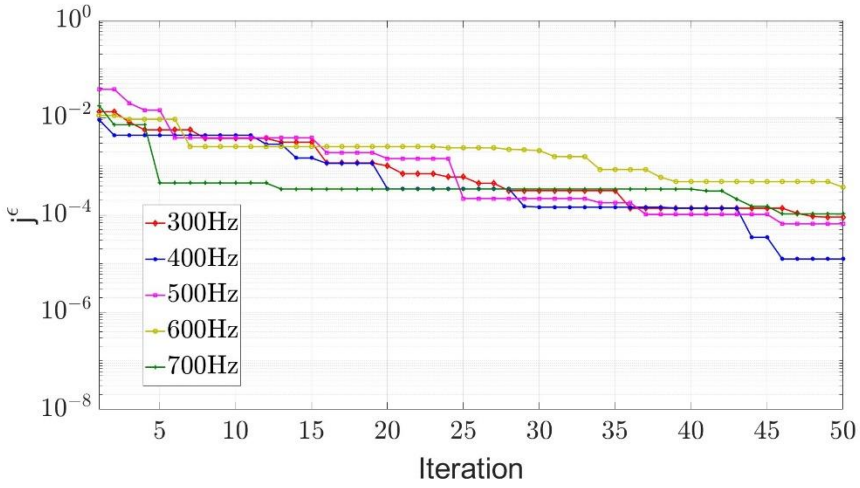

Figure 18: DE Behavior of Single Frequency Optimization with Smoothing

The optimizations with smoothing had the same plateau behavior. While there are a few periods for some of the frequencies that the plateau lasted for more than ten iterations, the smoothing had more frequent steps that the non-smooth cases.

Unlike the cases without smoothing, most of the smoothed cases required almost the entire 50 iterations to achieve the 10^{-2} to 10^{-4} reduction. This makes sense in context of smoothing, since out of all the possible shapes the DE algorithm could make, it is likely that more of these are not smooth, thus the probability of mutating to a smooth and well performing shape is low. The return on increasing the number of iterations was more significant than with the single-frequency optimization. The 700 Hz optimization achieved 88% reduction in back-reflection, which was the smallest decrease of the smoothing optimizations. 300 Hz optimization showed the greatest improvement, with 99.8% reduction.

4.7.3 Non-Smooth and Smooth Comparison

The square of the absolute value of the scattered field are shown in Fig.19 to Fig.23 for the non-smooth and smooth optimum design shapes found at 300-700 Hz frequencies.

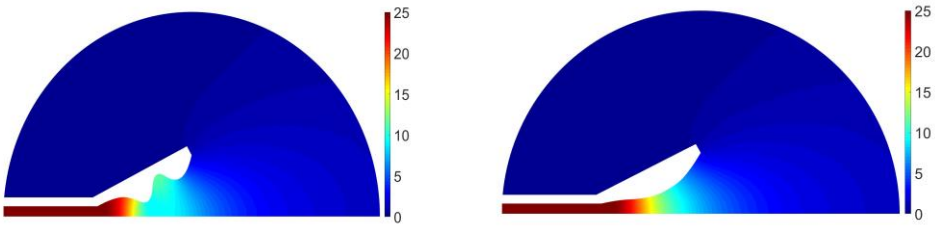

Figure 19: Non-Smooth and Smooth optimum design performance at 300Hz

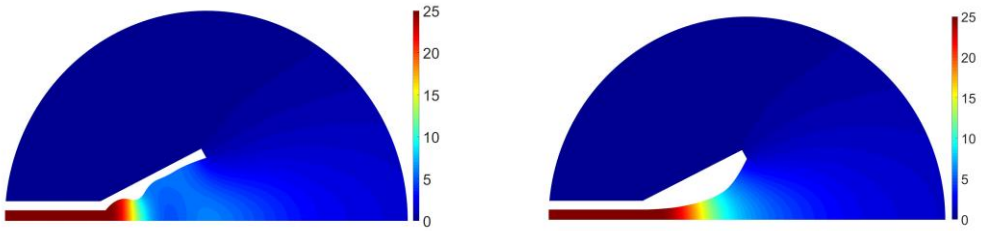

Figure 20: Non-Smooth and Smooth optimum design performance at 400Hz

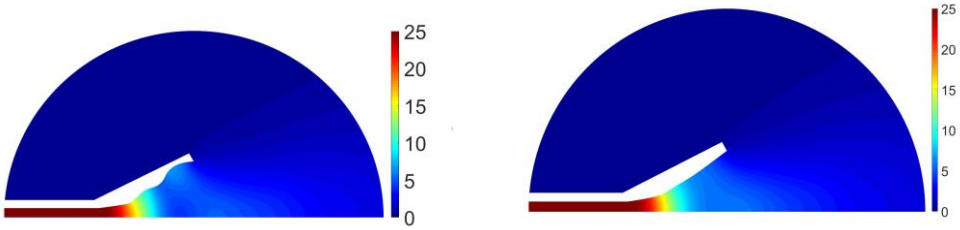

Figure 21: Non-Smooth and Smooth optimum design performance at 500Hz

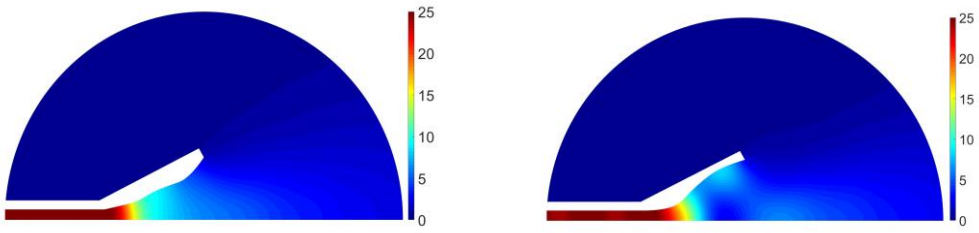

Figure 22: Non-Smooth and Smooth optimum design performance at 600Hz

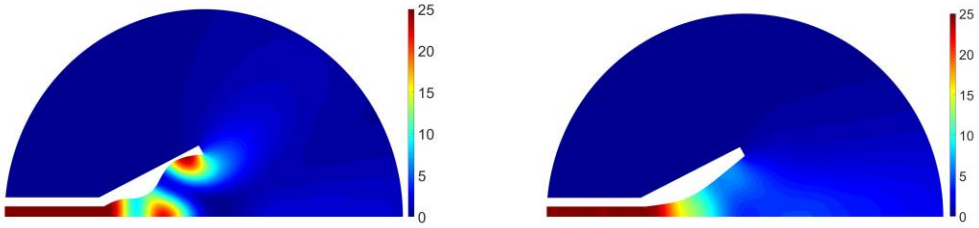

Figure 23: Non-Smooth and Smooth optimum design performance at 700Hz

4.8 Multi-Frequency Optimization

4.8.1 Multi-Frequency Setup

The single-frequency smoothing trials demonstrated that there may be a shape configuration that globally improves the performance of the horn across the entire 300 to 700Hz range.

The next optimization algorithm was set up to optimize the sum of objective function value *J* for each shape analyzed at the three frequencies of 300, 400, and 500Hz. The objective of this multi-frequency optimization is to find a single optimum horn shape for the above-mentioned frequencies. A similar method was used for a five-frequency optimization that is run to cover the entire range from 300 to 700Hz in steps of 100Hz. This is to determine if there is a shape that can globally reduce the back reflection for the full

range considered in this study. Both of these optimizations were performed with and without smoothing.

4.8.2 Multi-Frequency Results

The objective value *J* at each of the target frequencies for the multi-frequency optimizations are tabulated in Table 4.

Table 4: Multi-frequency optimization results

Frequency (Hz)	3-Freq. without smoothing *J*	3-Freq. with smoothing *J*	5-Freq. without smoothing *J*	5-Freq. with smoothing *J*
300	1.755e-04	7.331e-05	1.630e-03	1.923e-03
400	4.194e-05	2.119e-04	1.259e-04	6.000e-05
500	2.684e-04	1.506e-04	1.284e-04	1.695e-03
600	0.0044	0.0069	1.288e-04	3.174e-04
700	0.0103	0.0194	9.991e-04	7.020e-04

Without smoothing the 3-frequency optimization achieved a 98.3% average reduction in back-reflection at the three target frequencies, however at 600 Hz only a 45.5% reduction is achieved. At 700 Hz, the back-reflection is increased by over 1000%. With smoothing, 3-frequency optimization had an average of 97.4% reduction, but only 14% at 600 Hz and an increase of 2000% at 700 Hz.

The 5-frequency optimization without smoothing achieved an average of 72.5% back-reflection reduction. However, the back-reflection at 700 Hz is an 11% increase from the original horn design performance. With smoothing, 77.7% reduction of objective value

J was achieved, additionally back-reflection was reduced for all target frequencies. The smallest reduction was at 700 Hz, with a 22% decrease in objective function *J*.

The resulting shapes from the three and five frequency optimizations, with and without smoothing, are presented in Fig.24.

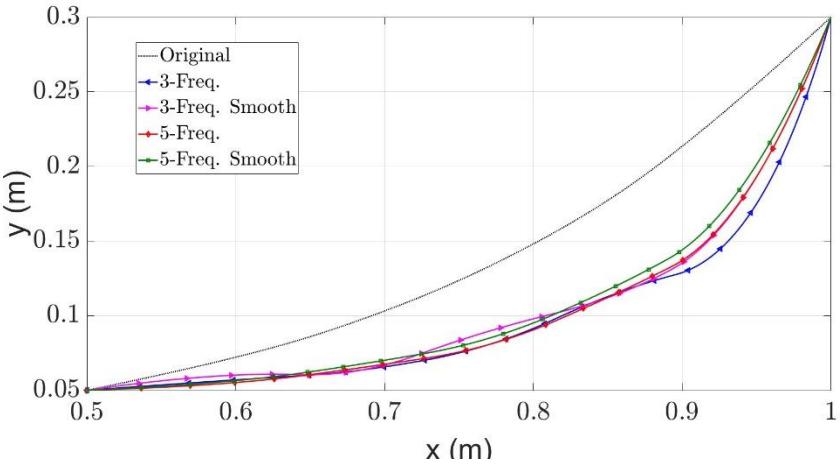

Figure 24: Comparison of Multi-Frequency Optimized Horn Bells

Interestingly, the shapes of all four cases of multi-frequency optimization are very similar, with very little difference between the shapes obtained with and without smoothing. The most notable outlier is the boundary found for three-frequency optimization without smoothing. In which the optimum shape becomes concave around x = 0.9m, then goes back to being convex, resulting in a ’bulge’ in the shape that is not present in the other cases. The performance of the optimum shapes found in reducing the back-reflection is compared in Fig.25 for the 300-700Hz range.

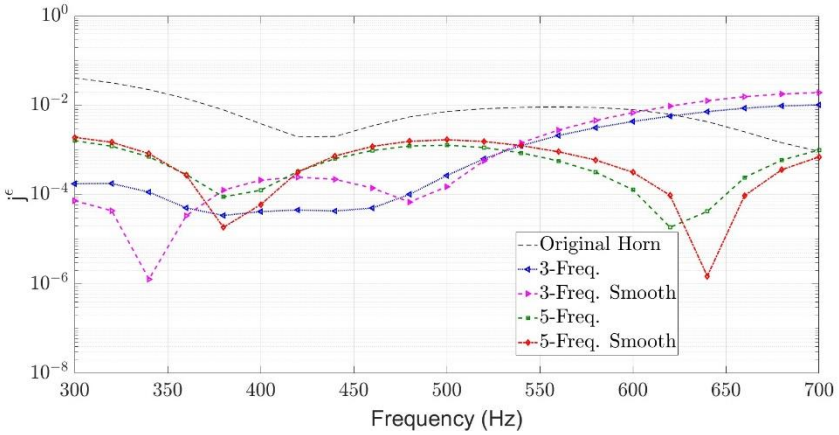

Figure 25: The comparison of the objective function value for the horn boundaries found using multi-frequency optimization

A close inspection of Fig.25 reveals that subtle differences between the optimum solution found significantly affects the resulting objective function *J* value and back reflection. Both of the three-frequency cases have results that improve upon the base horn's for that range, but both tended to performed worse in the range above 600Hz. Unlike the single frequency study, the smoothed three-frequency case resulted in a lower global minimum when compared to the non-smoothed shape. While this smoothed shape resulted in lower objective function *J* values in the 300 to 360Hz range, it was significantly higher in the 360 to 460Hz range. For the frequencies 480Hz and greater, the smooth and non-smooth had similar results. The objective function evaluated using five-frequency optimized boundary showed similar results, but the smoothed shape also yielded lower global minimum than the non-smooth case. Notably, the optimum solution found using five-frequency optimization both achieved a global reduction with the entire 300-700Hz frequency range's objective function *J* values.

The reduction of the objective function with the number of iterations is shown in Fig.26 for three and five frequency optimizations.

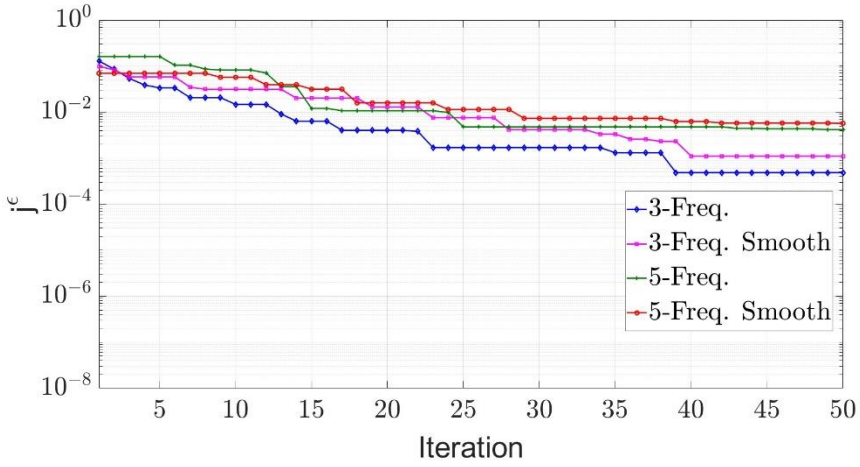

Figure 26: DE Behavior of Multi-Frequency Optimization

A close similarity is observed in objective function reduction with the number of iterations for multi-frequency optimization. Each optimization does plateau at around 40 iterations with no further decrease past that iteration. All four cases behaved similar to the smoothed single frequency cases, with many small decreases in the beginning, but the multi-frequency cases had no significantly large decreases between iterations. This could be an indication that across these ranges, the set of local optima shapes are generally very similar in performance.

For further comparison, Fig.27 to 28, present the numerical solution figures at their respective goal frequencies of the non-smooth shapes alongside the smooth shapes.

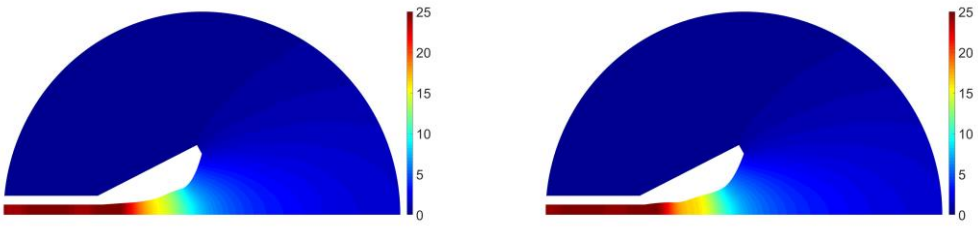

Figure 27: Non-Smooth and Smooth Numerical Solutions for 3-Frequency Optimization

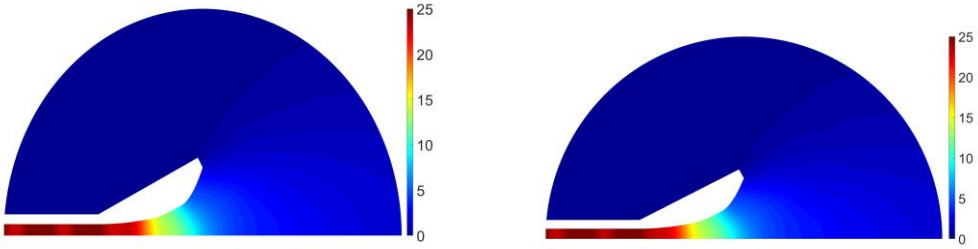

Figure 28: Non-Smooth and Smooth Numerical Solutions for 5-Frequency Optimization

Chapter 5

Sound Energy Harvesting

5.1 Overview

Another area in acoustics that has recently seen a lot of interest is sound energy harvesting. Sound energy harvesting is the process of converting acoustic wave energy to electric energy using a mechanical transducer. Many studies have investigated the transducer mechanism itself, developing a set of novel devices for converting the sound energy to an electric current [19][20][21]. Particularly, there is interest in harvesting ambient sound produced by road-noise and mass-transit [22][23].

A common method is to incorporate these energy harvesters into sound barrier walls that line roads and rails in residential areas [24][25]. Other ways of producing sound barriers have been found as an alternative to having a conventional solid wall. In particular, the use of a cylinder lattice, sometimes referred to as a sonic crystal, was studied as a more efficient and customizable solution [26][27].

This study investigates the potential of energy harvesting by incorporating a wave-guide structure into a cylinder, of a kind that might be used in a sonic crystal lattice and using shape optimization to improve the collection of sound energy within it.

5.2 Problem Formulation

Starting with the same wave equation given in Eq.17, writing p as $p(x,t) = u(x)e^{-i\omega t}$, leads to the Helmholtz equation [4]:

$$\Delta u + k^2 u = 0 \tag{40}$$

In this study, sound-hard material embedded in air medium is used and apply Neumann boundary condition on the surface of the scatter as described in Eq.41.

$$u = g \quad \text{on} \quad \Gamma_D \tag{41}$$

where n is the normal vector on Γ pointing outward and u^{inc}:

$$g = -u^{inc} \qquad ikh = -\frac{\partial u^{inc}}{\partial n} \qquad f = -\frac{\partial u^{inc}}{\partial n} - \alpha u^{inc} \tag{42}$$

Since this is an exterior acoustic problem the computational domain should be truncated with an Absorbing Boundary Condition (ABC). To allow the wave to propagate into infinite space with minimum reflection. In this case, second order Bayliss-Turkel ABC (BGT-2 ABC) is chosen, which provides adequate accuracy with minimal computational cost and has been applied in many previous IGA-acoustics studies [28]. Hence the following boundary condition is applied on the outer boundary

$$\frac{\partial u}{\partial n} + \mathbf{B}u = 0 \quad \text{on} \quad \Sigma \tag{43}$$

where B is the linear operator referred to as Dirichlet-to-Neumann map. For BGT-2 type ABC, one has [29]:

$$\mathbf{B}u = (-ik + \frac{\kappa}{2} - \frac{\kappa^2}{8(\kappa - ik)})u - \frac{1}{2(\kappa - ik)}\frac{\partial^2 u}{\partial s^2} \tag{44}$$

With Σ being the fictitious boundary represented by a circle with radius R and $\frac{\partial u}{\partial n} = \frac{\partial u}{\partial r}$, with $\kappa = 1/R$ and the tangential derivative $\frac{\partial^2 u}{\partial s^2} = \frac{1}{R}\frac{\partial^2 u}{\partial \theta^2}$ in polar coordinates (r,θ).

The weak form then is obtained by multiplying Eq.40 by a test function *v* and integrating over Ω, then applying the boundary conditions in Eq.41:

$$a(u,v) = l(v), \qquad \forall V \tag{45}$$

$$a(u,v) = \int_{\Omega} \nabla u \nabla v d\Omega - k^2 \int_{\Omega} uvd\Omega + \alpha \int_{\Gamma_d} uvd\Gamma + \int_{\Sigma} \mathbf{B}uvd\Gamma \tag{46}$$

$$l(v) = \int_{\Gamma_N} hvd\Gamma + \int_{\Gamma_R} fvd\Gamma \tag{47}$$

5.3 Problem Setup

Consider the 2D cross section of the proposed cylindrical sound harvester within the circular domain, Ω, considered in Fig.29 where the computational domain and the close up of the harvester are shown in left and right respectively. The maze structure of the proposed solid-walled harvester is placed within an empty space assumed to have the properties of air illuminated by a plane wave traveling from left to right. The outer circle, Σ, is the fictitious boundary on which ABC was applied.

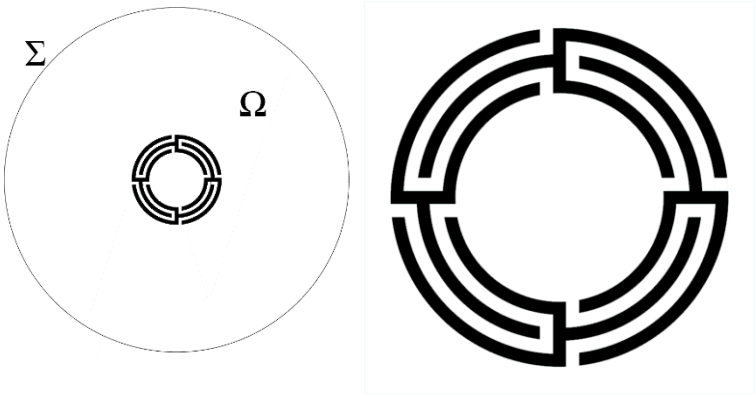

Figure 29: Harvester Full Domain and Zoomed view

Similar maze meta-surfaces were studied for noise reduction purposes in an ultra-sparse arrangement [30][31]. The sound wave can travel through the maze between the solid walls which are depicted by black walls in Fig.29. In this study the possibility of tuning and enhancing the performance of the proposed energy harvester by shape optimization was investigated. The four design variables used for shape optimization were: wall width w_h, entire maze channel width c_h, harvester rotation θ_h, and "wing" rotation θ_w, the variables are shown in Fig. 30, R_{int} denotes the interior harvester radius.

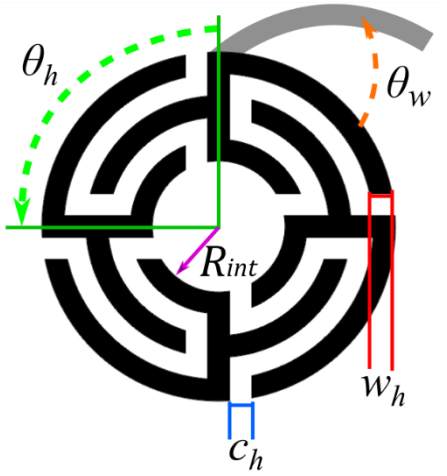

Figure 30: Harvester shape modification variables

To demonstrate the scalability of the proposed harvester the optimized design performance was compared with the initial design performance for a range of frequencies. In the initial design, the following parameter values were used: $w_h = c_h = 0.002$, $\theta_h = 0$, and $\theta_w = 0$. Three main shape optimizations were considered. In the first type only channel and wall thickness were allowed to change. This limited shape optimization is demonstrated in Fig. 31 and Fig.32 where the channel width c_h and wall width w_h were increased respectively. Due to increasing c_h and w_h, the total radius of the harvester decreased.

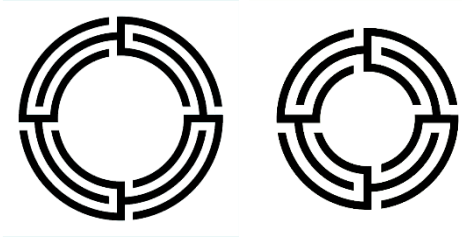

Figure 31: Initial harvester (left) compared to harvester with increased c_h (right)

Increasing the channel width as shown in Fig. 31 widens the acoustic wave passage channel. Increasing the wall width does not affect the channel size but does change the total radius along with total passage length.

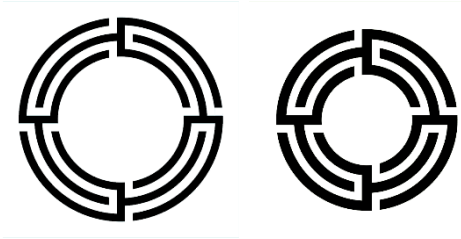

Figure 32: Initial harvester (left) compared to harvester with increased w_h (right)

Another possibility is to rotate the harvester to find the optimum placement angle. This is demonstrated in Fig.33.

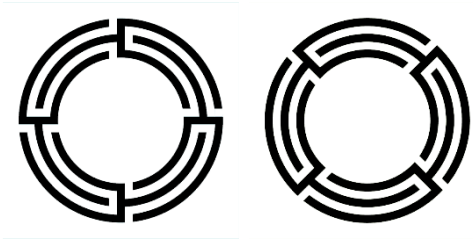

Figure 33: Initial harvester (left) compared to rotated harvester (right)

Additionally, the harvester can undergo what will be referred to as ”wing movement” hereafter which is the outward rotation of the exterior channel wall. This opens up the main

point of entry for the wave, generates a varying channel width, and as extends the shape out more into the propagation domain. An example of this is shown in Fig.34.

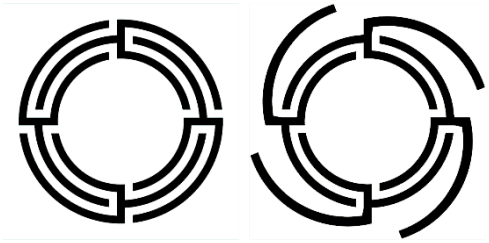

Figure 34: Initial harvester (left) compared to harvester with wing movement (right)

The objective function of this optimization is the sum of the pressure within the area defined by R_{int}, divided by the interior area. The objective function is denoted as J_H, which is defined as:

$$J_H = \frac{\sum P_{rad}}{R_{int}{}^2 * \pi} \tag{48}$$

With P_{rad} as the pressure at a point within $R_{int.}$

The following optimizations were performed for the range of 500 to 700Hz in steps of 100Hz:

- Optimize w_h and c_h while fixing $\theta_h = \theta_w = 0$
- Optimize w_h,c_h , and θ_h while fixing $\theta_w = 0$
- Optimize w_h, c_h, θ_h and θ_w

In all the above optimizations w_h and c_h were allowed to vary between 0.001 and .005 meters, while θ_h and θ_w were allowed to vary between 0 and $\pi/2$. The IGA mesh was

composed of 59 patches similar to the one shown in Fig.35, where $w_h = c_h = 0.04$ and $\theta_h = \theta_w = 0$:

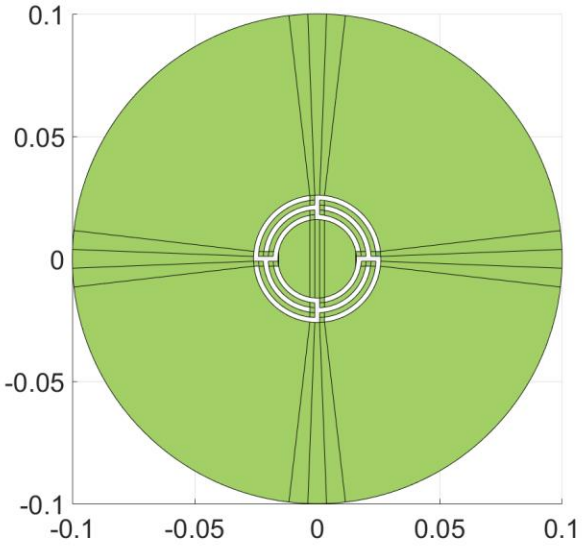

Figure 35: Multi-patch mesh of the initial harvester design

The J_H values at the target frequencies are tabulated in Table 5

Table 5: Initial Harvester Design Target Frequency J_H values

Frequency (Hz)	500	600	700	800	900	1000
J_H	2416	13187	1651	1112	539	396

From Table 5 it is apparent that the initial harvester design is better suited for 600 Hz than any of the other target frequencies.

5.4 Shape Optimization of the Sound Energy Harvester Results

5.4.1 Channel and Wall Modification

The first optimization for the sound harvesting case was performed using only w_h and c_h. These two in combination will affect the radius of the harvester and the total length of the channels. The results from this optimization are listed in Table 6:

Table 6: w_h and c_h Optimization Results

Frequency (Hz)	w_h	c_h	J_H
500	0.0360	0.0389	26890
600	0.0300	0.0484	14925
700	0.0472	0.0383	16776
800	0.0386	0.0493	9241
900	0.0531	0.0385	12972
1000	0.0640	0.0308	11784

The highest value of the objective function was found for the 500Hz optimization in which J_H = 26890. The minimum objective function value was found for 800Hz which was only about 34% of that value, J_H = 9241. However, the next highest after 500Hz was the 700Hz optimization, which reached J_H = 16776, only 62% of the 500Hz result. The 600 Hz optimization achieved a 13.2% increase of J_H, which was the smallest percent increase, however the 1000 Hz optimization had a 2875% increase of the objective function value J_H. The average increase achieved by the optimizations was 1309%.

Figure 36 depicts the value of the objective function for the optimum designs found in the range of 400-1100 Hz frequencies.

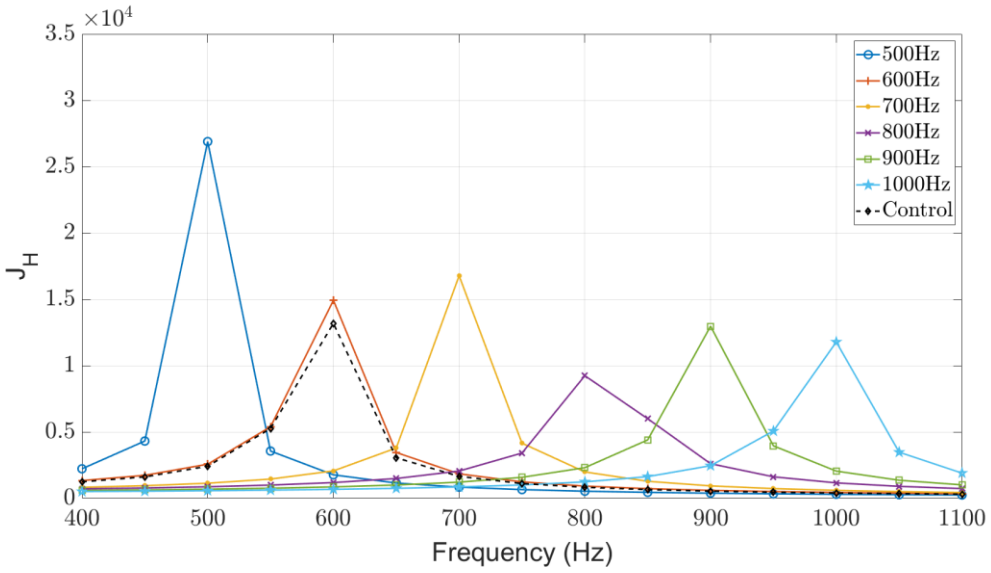

Figure 36: Spectrum performance of optimized harvesters (w_h,c_h)

It is clearly seen that each of the optimum solutions found have similar performance as shown in Fig.36, a sudden sharp spike is observed at the targeted frequency with similar declination on either side. The only design which significantly deviates from this pattern is the one obtained for 800Hz optimization. At 850Hz it is almost double the value of 750Hz for the same harvester configuration. Interestingly the initial design was effective at 600Hz and consequently the optimization improved the performance slightly at this frequency.

The resulting shapes and corresponding total field are shown in Fig.37 to 42, for their respective objective frequencies. The increased red within the optimized harvester interior compared to the initial design is a clear indication that the shape optimization achieved increased pressure concentration within the harvester.

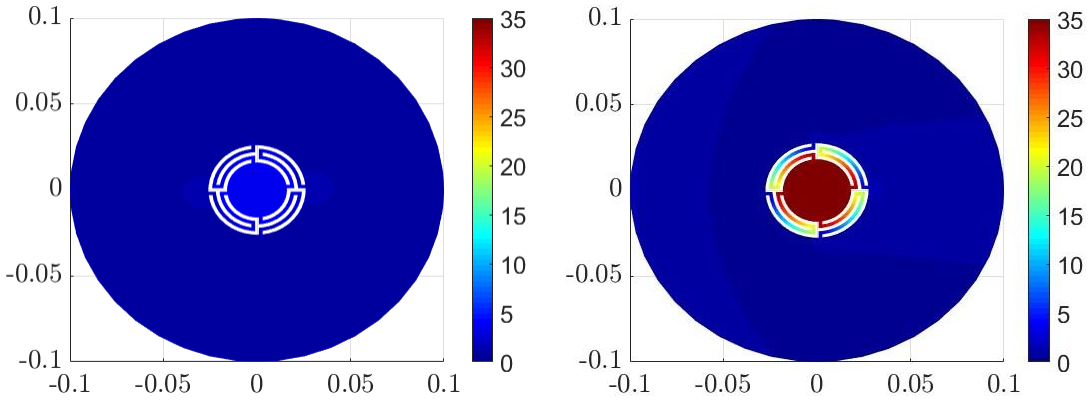

Figure 37: Pressure field at 500Hz for initial (left) and optimized harvester (right) (w_h,c_h)

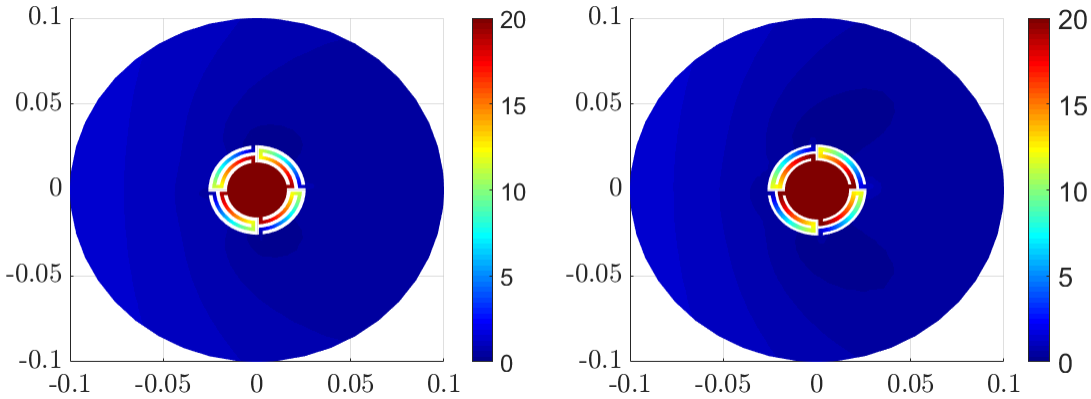

Figure 38: Pressure field at 600Hz for initial (left) and optimized harvester (right) (w_h,c_h)

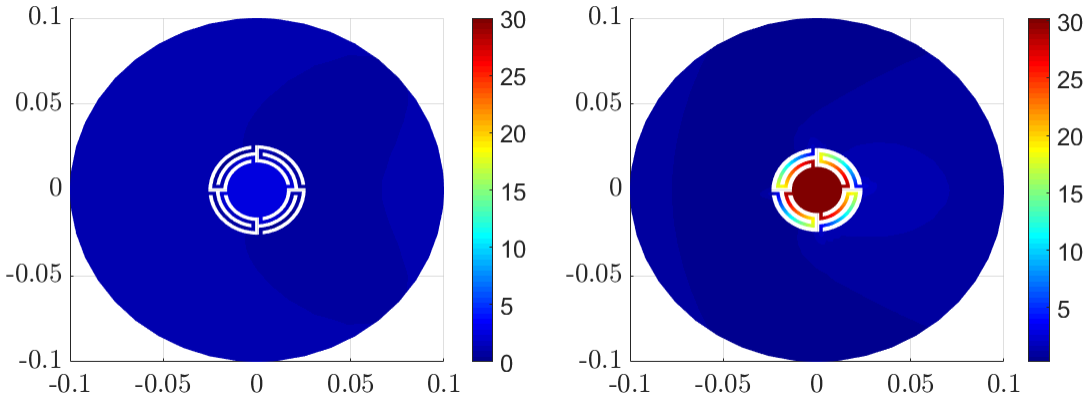

Figure 39: Pressure field at 700Hz for initial (left) and optimized harvester (right) (w_h,c_h)

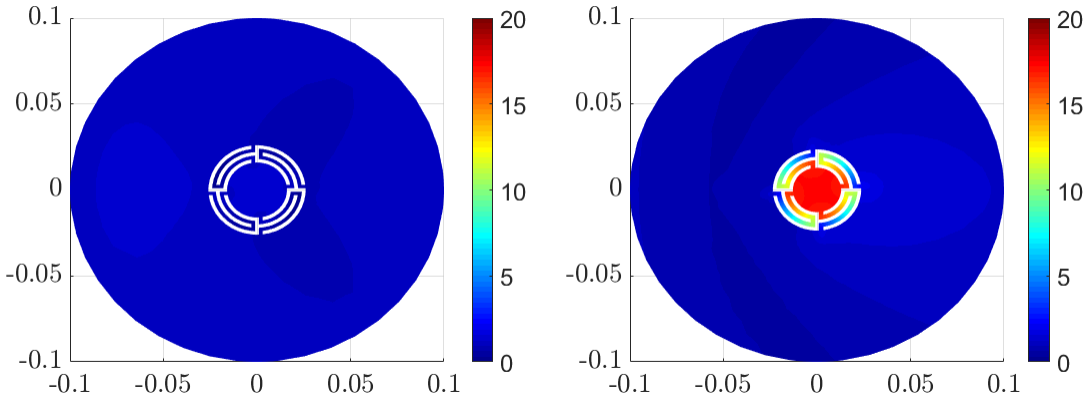

Figure 40: Pressure field at 800Hz for initial (left) and optimized harvester (right) (w_h,c_h)

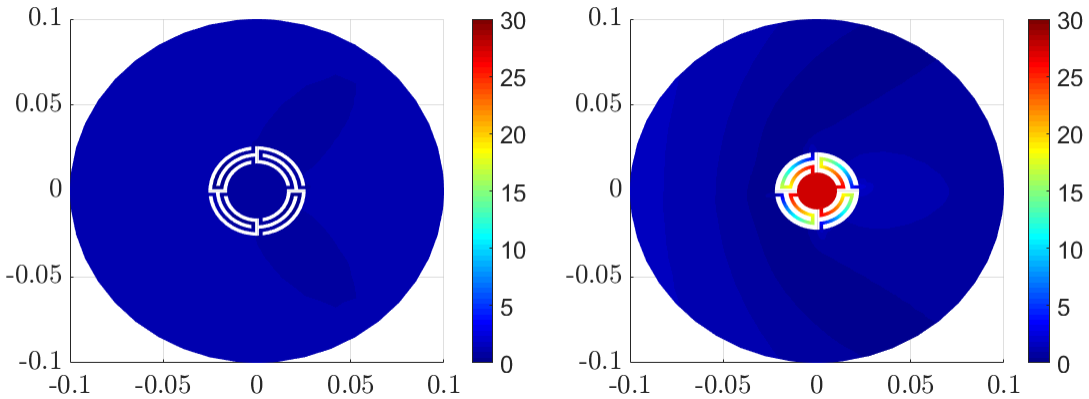

Figure 41: Pressure field at 900Hz for initial (left) and optimized harvester (right) (w_h,c_h)

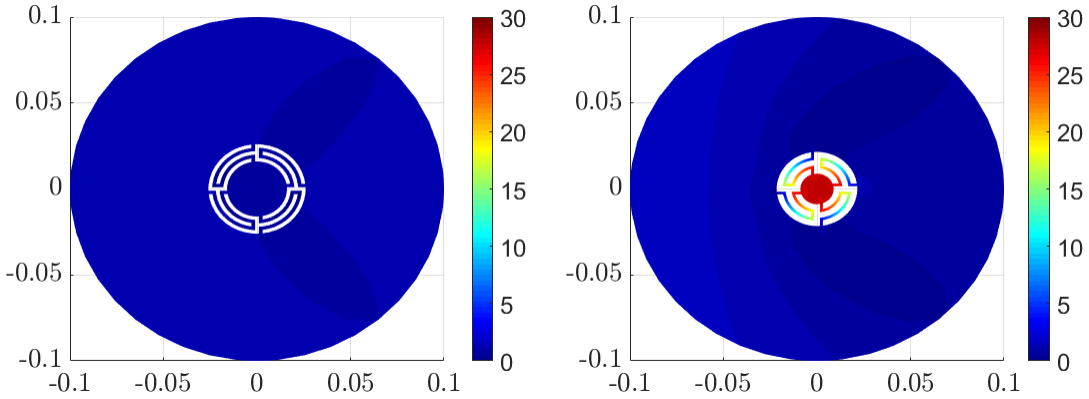

Figure 42: Pressure field at 1000Hz for initial (left) and optimized harvester (right) (w_h,c_h)

From Figure 37 to Fig.42, the interior radius of the optimized harvesters decreases as the target frequencies increase. The only exception to this is between the 700Hz and 800Hz optimizations, where the interior radii are similar.

The DE performance of the optimization is shown in Fig.43. This chart tracks the objective value achieved by each iteration.

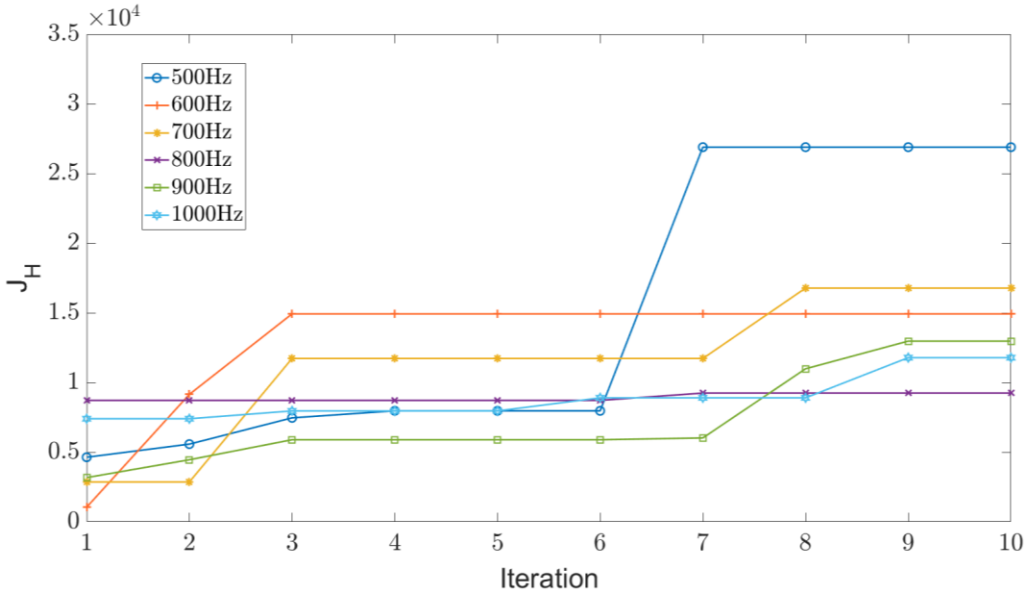

Figure 43: Iteration History of Optimization (w_h,c_h)

The DE performance showed many plateaus with most of the steps being small, the 500Hz objective had the largest step, going from under 1000 to over 2500 in a single iteration.

5.4.2 Channel, Wall Modification, and Rotation

The next optimization was to include the rotation of the harvester, θ_h as an additional design variable. The results of the optimization performed for each target frequency are shown in Table 7:

Table 7: w_h, c_h, and θ_h Optimization Results

Frequency (Hz)	w_h	c_h	θ_h	J_H
500	0.0242	0.0480	1.1771	18910
600	0.0425	0.0386	1.1712	20740
700	0.0588	0.0286	1.2399	19267
800	0.0320	0.0553	0.5699	9520
900	0.0751	0.0200	0.0000	14762
1000	0.0767	0.0200	0.0000	13900

The reduced objective function for the 500Hz optimization is an indication that a local optimum is found instead of than the global optimum. DE is recognized as a method which successfully find the global minimum, but it does not eliminate such possibility.

These optimizations yielded increases in J_H values between 57% at 600 Hz and 3410% at 1000 Hz. The average increase achieved by the optimizations was 1435%.

Figure 44 charts the behavior of each harvester over the frequency spectrum of 400 to 1100Hz.

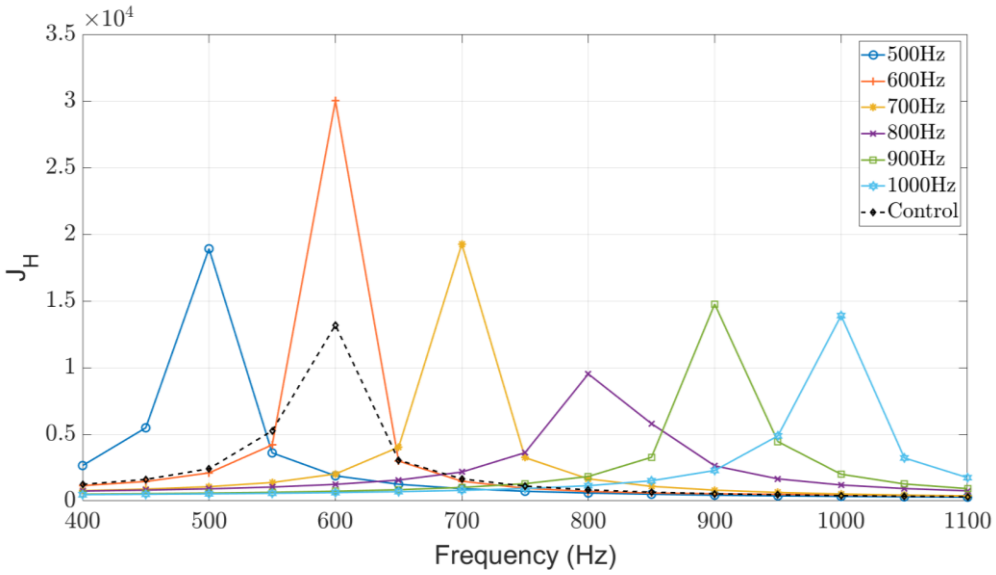

Figure 44: Spectrum Performance of optimized harvesters (w_h,c_h,θ_h)

Another interesting behavior is that there is very little change between the first optimization and the result once θ_h is included for the range of 800 to 1000Hz. Those three frequencies also had the smallest amount of rotation, with 900 and 1000Hz having no rotation at all. The 600 Hz target frequency showed significant improvement with the addition of θ_h as a design variable. The 500 Hz and 600Hz optimizations have similar rotation.

The resulting shapes and corresponding pressure fields are shown in Fig.45 to 50, for their respective objective frequencies.

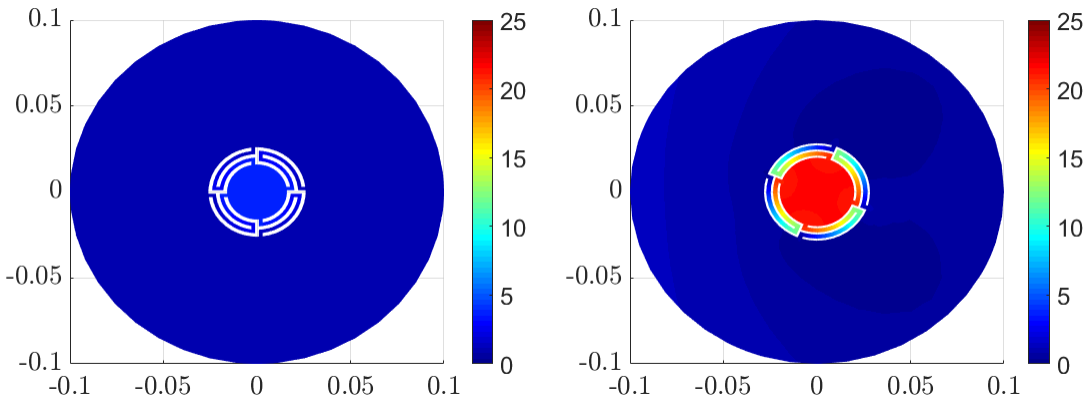

Figure 45: Pressure field at 500Hz for initial (left) and optimized harvester (right) (w_h,c_h,θ_h)

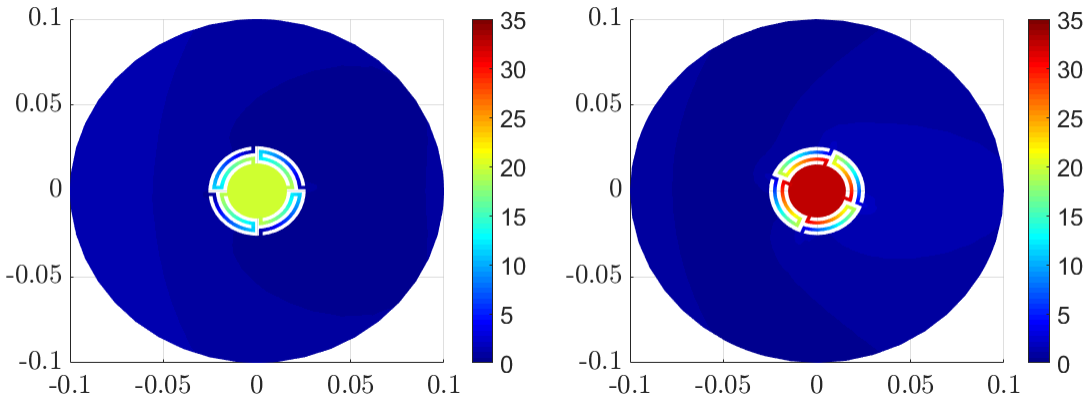

Figure 46: Pressure field at 600Hz for initial (left) and optimized harvester (right) (w_h,c_h,θ_h)

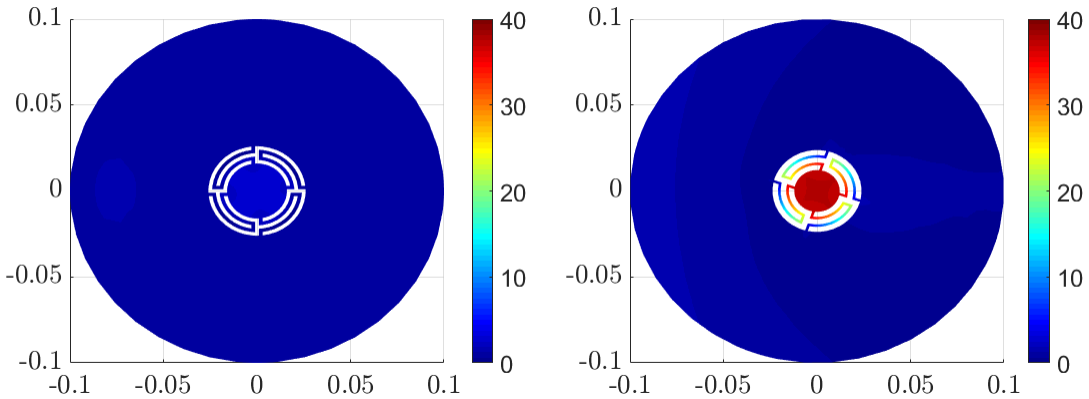

Figure 47: Pressure field at 700Hz for initial (left) and optimized harvester (right) (w_h,c_h,θ_h)

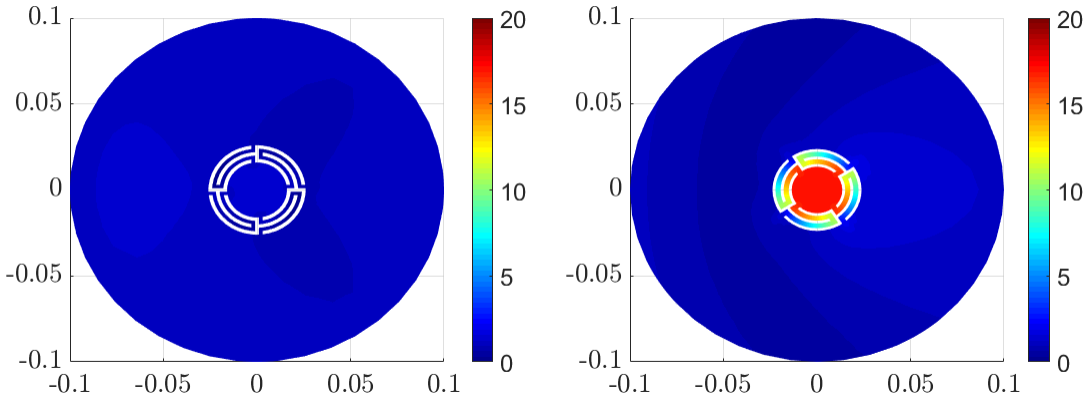

Figure 48: Pressure field at 800Hz for initial (left) and optimized harvester (right) (w_h,c_h,θ_h)

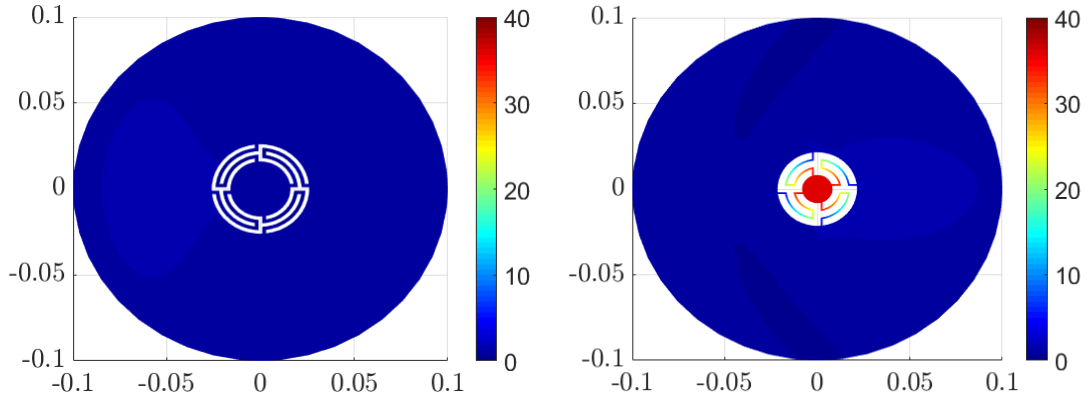

Figure 49: Pressure field at 900Hz for initial (left) and optimized harvester (right) (w_h,c_h,θ_h)

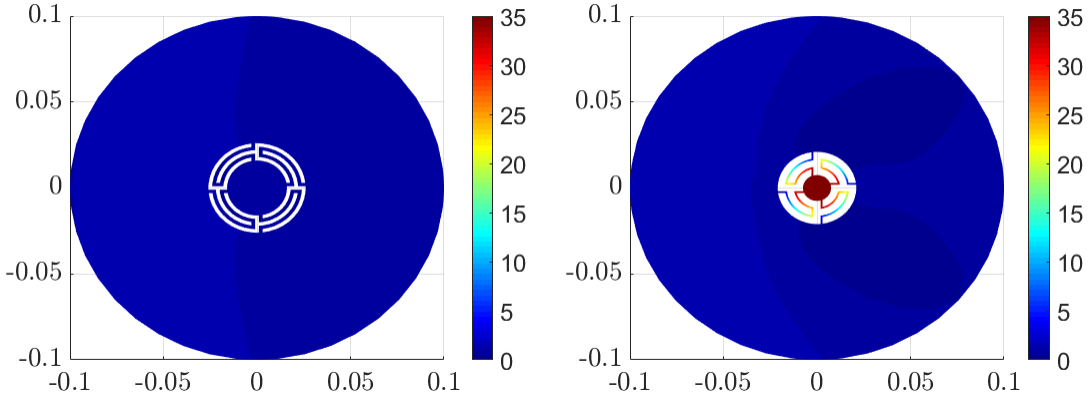

Figure 50: Pressure field at 1000Hz for initial (left) and optimized harvester (right) (w_h,c_h,θ_h)

These optimizations tend to produce smaller interior radii as the frequency increases, similar to the previous optimizations. In addition, the 700 Hz to 800 Hz is an outlier to this trend. With rotation included in the shape optimization variables, the 800 Hz optimized harvester has a larger interior radius than the 700 Hz optimized harvester. The DE performance is shown in Fig.51.

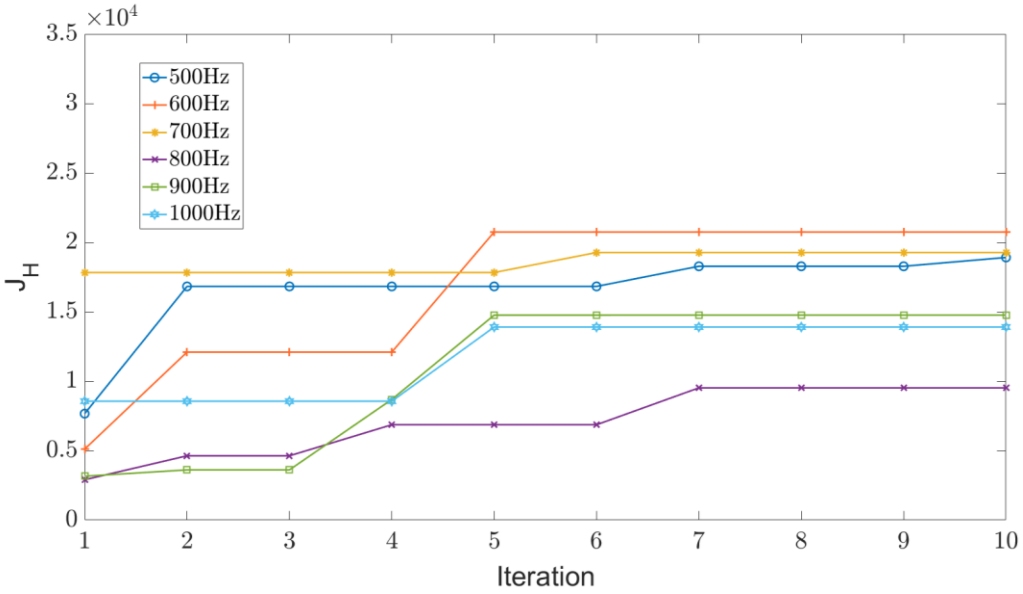

Figure 51: Iteration History of Optimization (w_h,c_h,θ_h)

Almost all of these optimizations were on a plateau at the end of iteration 10. The 700Hz optimization only had a single increase, between iteration 5 and 6. Increasing the number of iterations may improve the results obtained.

5.4.3 Channel, Wall Modification, Rotation, and Wing Movement

The results for the optimizations with wing movement included are listed in Table 8.

Table 8: w_h, c_h, θ_h and θ_w Optimization Results

Frequency (Hz)	w_h	c_h	θ_h	θ_w	J_H
500	0.0531	0.0200	1.569	0.4622	33002
600	0.0578	0.0200	0.8836	0.9480	25584
700	0.0459	0.0315	1.0300	0.8202	14916
800	0.0529	0.0286	0.8765	1.4810	13171
900	0.0438	0.0385	1.5710	1.5710	11319
1000	0.0461	0.0393	1.3620	1.1580	9723

The addition of wing movement to the optimization only yielded higher values of J_H than the previous optimizations for the target frequencies 500 Hz, 600 Hz, and 800 Hz. Interestingly, none of these optimizations had no rotation or no wing movement.

These optimizations yielded increases in J_H values between 94% at 600 Hz and 2355% at 1000 Hz. The average increase achieved by the optimizations was 1267%.

Figure 52 charts the behavior of each harvester over the frequency spectrum of 400 to 1100Hz.

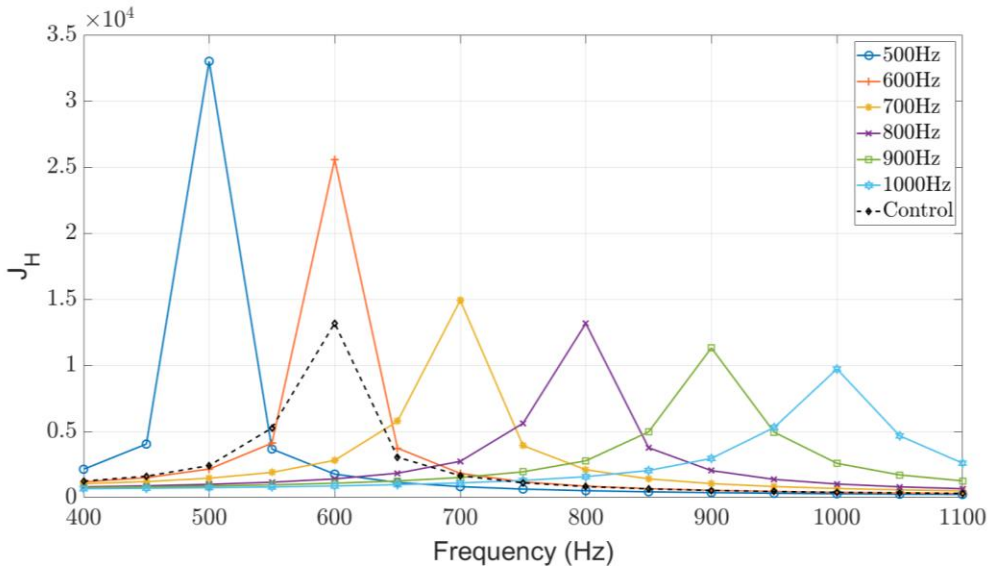

Figure 52: Spectrum Performance of optimized harvesters (w_h,c_h,θ_h,θ_w)

The resulting shapes and corresponding total field are shown in Fig.53 to 58, for their respective objective frequencies.

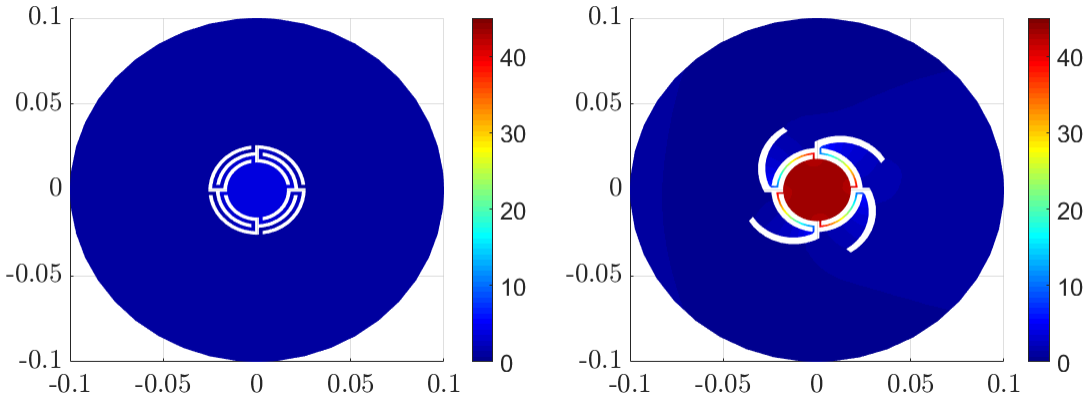

Figure 53: Pressure field at 500Hz for initial (left) and optimized harvester (right) (w_h,c_h,θ_h,θ_w)

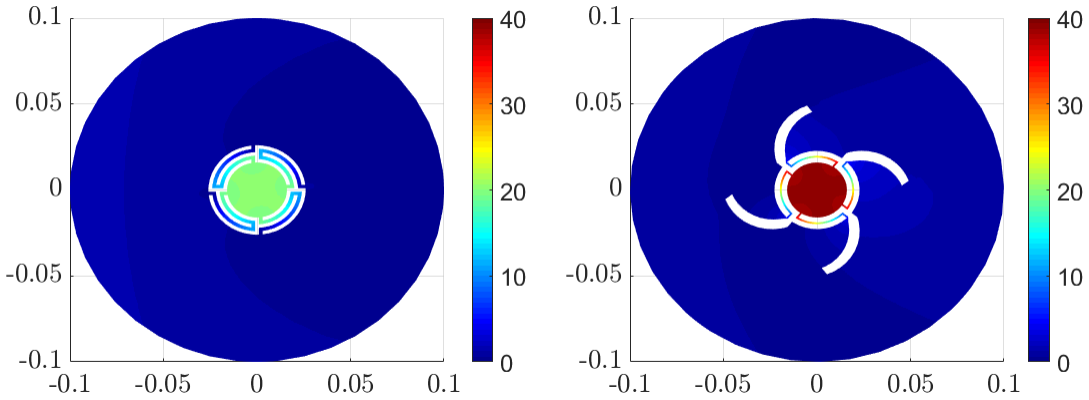

Figure 54: Pressure field at 600Hz for initial (left) and optimized harvester (right) (w_h,c_h,θ_h,θ_w)

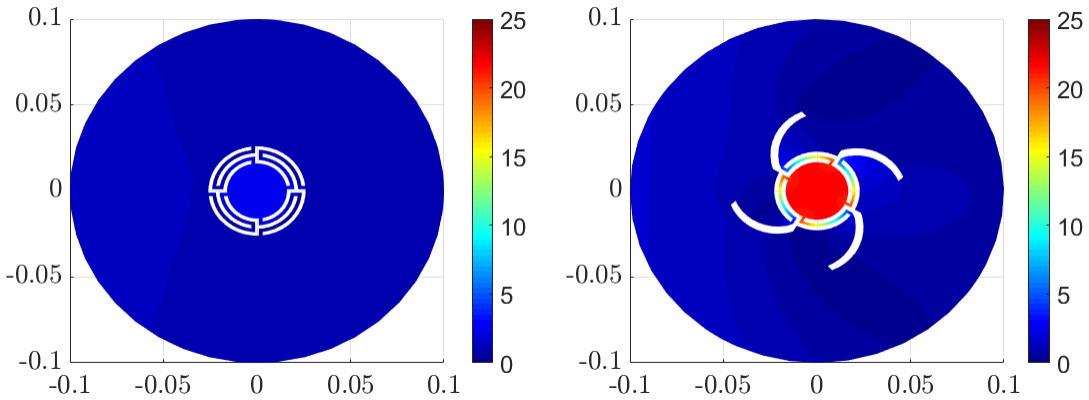

Figure 55: Pressure field at 700Hz for initial (left) and optimized harvester (right) (w_h,c_h,θ_h,θ_w)

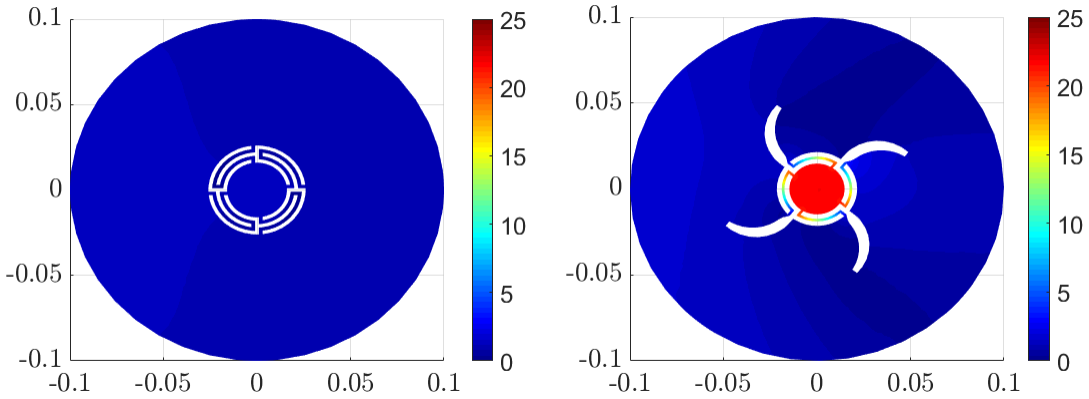

Figure 56: Pressure field at 800Hz for initial (left) and optimized harvester (right) (w_h,c_h,θ_h,θ_w)

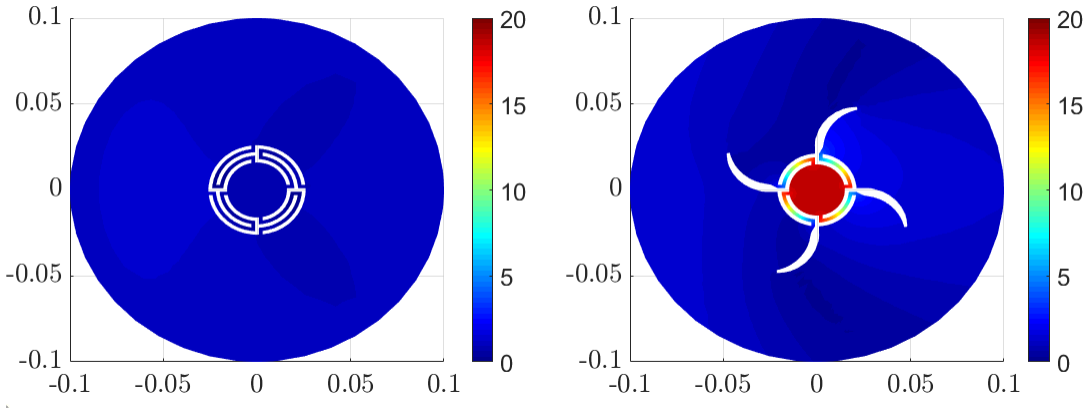

Figure 57: Pressure field at 900Hz for initial (left) and optimized harvester (right) (w_h,c_h,θ_h,θ_w)

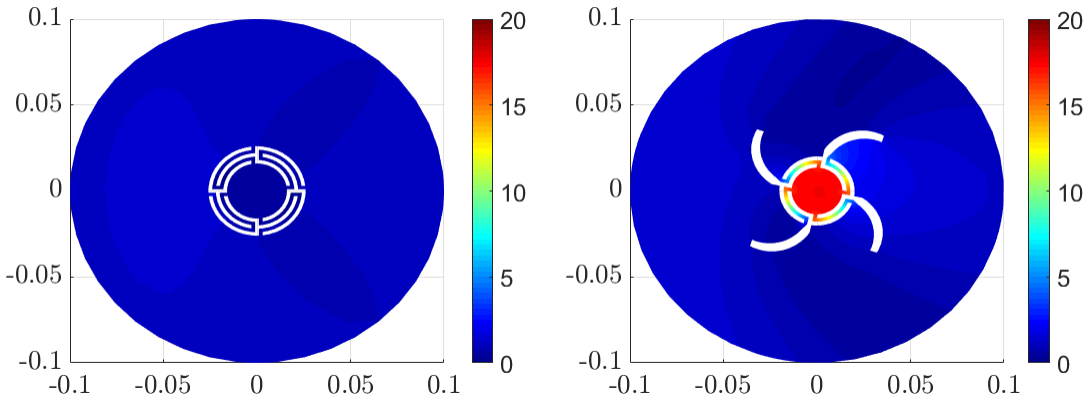

Figure 58: Pressure field at 1000Hz for initial (left) and optimized harvester (right) (w_h,c_h,θ_h,θ_w)

The DE performance is of the optimizations are shown in Fig.59. Most of these runs showed little improvement over 10 iterations, with the exception of 500Hz, which showed steady and significant increases until iteration 7. The 600Hz run did not improve throughout the entire process. Interestingly, like the previous optimizations, the interior radius of the harvester decreased as the target frequency increased. However, the reduction is much less significant than before.

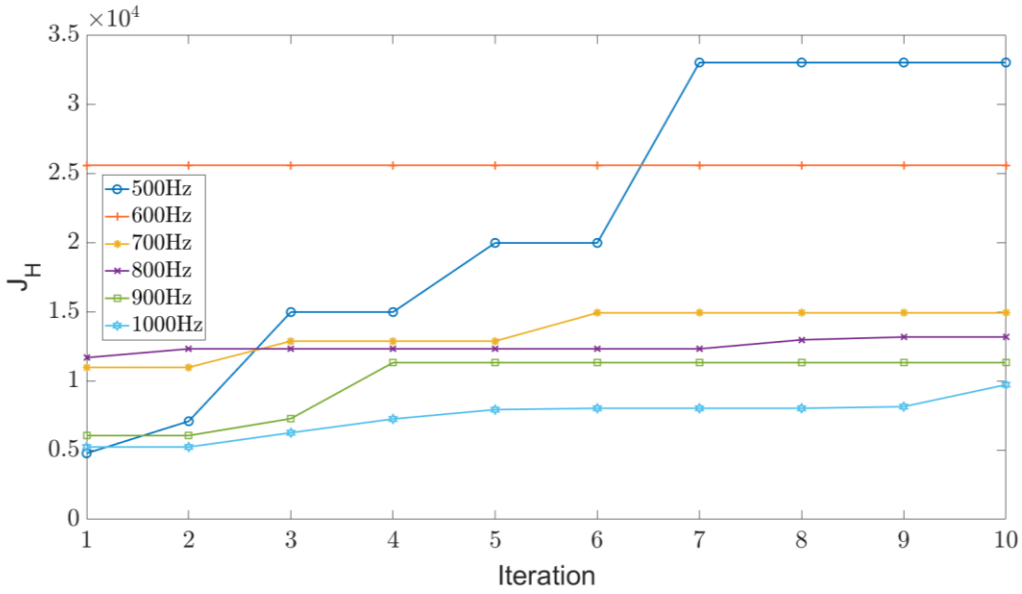

Figure 59: Iteration History of Optimization (w_h,c_h,θ_h,θ_w)

Chapter 6

Conclusion

6.1 Summary

In this thesis, two applications of acoustic optimization utilizing the combination of IGA and DE where studied. IGA provides a convenient high order numerical framework for performing analysis with less computational cost at similar accuracy to conventional FEA [5][32]. It can also reduce the burden of re-meshing when compared to conventional FEA. DE is chosen as the preferred evolutionary algorithm for optimization due to its speed and capability to find the optimum solution more successfully.

The first optimization problem considered in this study reduced the back-reflection in an acoustic horn speaker for the frequency range of 300 Hz to 700 Hz. Back-reflection causes interference and possibly cancellation on the outgoing acoustic wave. To reduce this effect, the shape of the horn bell was optimized. Optimizations were successfully performed for both single and multiple target frequencies. Not all the solutions found were smooth and easy to manufacture. Smooth optimum boundaries were found for all frequencies considered using Tikhonov regularization, which was utilized to penalize complex optimum shapes.

Without smoothing, single-frequency optimization achieved between 99.60% to 99.99% reduction in back-reflection for each of the target frequencies. The average reduction of objective function value, J, was 99.90%. With smoothing, back-reflection was reduced between 88.3% and 99.8%. The average decrease in back-reflection for the optimizations with smoothing was 96.4%.

The 3-frequency optimization for the three target frequencies of 300 Hz, 400 Hz and 500 Hz yielded an average reduction of 98.3% without smoothing and 97.4% with smoothing. 5-frequency optimization for target frequencies of 300 Hz, 400 Hz, 500 Hz, 600 Hz and 700 Hz, with and without smoothing achieved average back-reflection reduction of 75.5% and 77.7% respectively.

The second case studied was the shape optimization of a proposed sound-energy harvester. The objective of the optimization is to increase the pressure within cylindrical sound-harvester by modifying a set of design variables.

The first optimizations of the harvester shape altered only the wall thickness and channel width to maximize the internal pressure. An average pressure increase of 1309% was achieved with only these two parameters. Including the rotation of the harvester for the next set of optimizations resulted in an average increase of 1435%. The addition of wing movement to the harvester design optimizations yielded an average increase of the objection function value J_H of 1267%.

6.2 Discussion

The acoustic horn shape optimization demonstrated that many of the optimal shapes were non-intuitive and that very subtle variations in the shape of the horn bell can have significant effect on the back-reflection. Without smoothing, the optimizations achieved lower amounts of back-reflection than with smoothing, however, the smoothed shapes would impose significantly less manufacturing constraints than the non-smooth shapes.

Interestingly, multi-frequency optimization of the acoustic speaker produced smooth shapes without the inclusion of smoothing. Indicating that smooth shapes are inherently more effective for a range of frequencies.

For each of the horn shape optimization cases, DE would plateau for many iterations. Most of the optimizations, both single and multi-frequency, were in a plateau by the final iteration. While improved results may be obtained through increasing the number of iterations, this would increase the computational time of the optimization. However, as most of the optimizations achieved above a 95% reduction in back-reflection by iteration 50, the improvement obtained by increasing the number of iterations may not be significant enough to warrant the additional computational time.

The proposed sound-energy harvester optimizations achieved significantly improved results compared to the initial design. An average increased pressure of over 1000% for all cases. This increase however can be seen as tuning the design for a target frequency by shape optimization.

The optimization of channel width, wall thickness and rotation yielded the highest average pressure increase percentage. This case also achieved a maximum J_H value compare to the other cases for the target frequencies of 700 Hz, 900 Hz and 1000 Hz. The inclusion of wing rotation achieved maximum J_H values at 500 Hz, 600 Hz and 700 Hz. However, with wing rotation the average increase was lowest, at 1267%. This might be related to reduced channel length.

Wing movement also increases the area occupied by the harvester, as the wings extend out into the domain. It would be much more difficult to place these in a sonic crystal-

lattice formation. For these reasons, wing movement may not be an ideal shape design variable to optimize without increasing the channel length.

6.3 Future Work

These studies lay the foundation for further optimization cases using IGA and DE. Additional parameters can be defined as design variables in the horn problem. Optimization including the width of the wave guide and a rotation of the horn bell might be factors that enhance the performance of the optimization.

Perhaps some modification to the objective function or optimization parameters could be made in the sound harvesting problem. There may be a method of re-defining the setup as to prevent the optimization towards a local optimum. Additionally, optimization cases using more iterations should be considered. Further high-frequency optimization could also expand the benefits of this study. The frequency ranges covered in this thesis are on the lower end of the human hearing range, so expanding toward the full range could provide additional benefit, especially considering that road noise also covers the entire hearing spectrum as well. Physical experiments to help verify these studies should also be performed.

Most importantly, this study demonstrated the potential for IGA and DE in the future development of devices relying on acoustic wave propagation. Another interesting study is to compare cost-benefit of using DE with optimization algorithms.

References

[1] L. Pegolotti, L. Dedè and A. Quarteroni. *Isogeometric Analysis of the electrophysiology in the human heart: Numerical simulation of the bidomain equations on the atria.* Comput. Methods Appl. Mech. and Engrg., 343:57-73, 2019.

[2] E. Bängtsson, D. Noreland and M. Berggren. *Shape optimization of an acoustic horn.* Comput. Methods Appl. Mech. and Engrg., 192:1533–1571, 2003.

[3] S. Morganti, F. Auricchio, D. Benson, F.I. Gambarin, S. Hartmann, T.J.R. Hughes and A. Reali *Patient-specific isogeometric structural analysis of aortic valve closure*. ICES REPORT 14-10, The Institute for Computational Engineering and Sciences, The University of Texas at Austin, May 2014.

[4] T. Khajah, X. Antoine and S. Bordas *B-spline FEM for time-harmonic acoustic scattering and propagation*. Comput. Acoust., 2018.

[5] J. Videla, C. Anitescu, T. Khajah, S. Bordas and E. Atroshchenko *h- and p- adaptivity driven by recovery and residual-based error estimators for PHT-splines applied to time-harmonic acoustics*. Computers and Mathematics with Applications, 77:2369-2395, 2019.

[6] R. Storn and K. Price *Differential Evolution - A Simple and Efficient Heuristic for Global Optimization over Continuous Spaces*. Journal of Global Optimization, 11:341-359, 1997.

[7] D. Karaboğa and S. Ökdem *A Simple and Global Optimization Algorithm for Engineering Problems: Differential Evolution Algorithm*. Turk J Elec Engin, 12, 2004.

[8] Les Piegl and Wayne Tiller. *The NURBS Book*. Springer, 1995.

[9] D.F. Rogers. *An Introduction to NURBS with Historical Perspective*. Academic Press, 2001.

[10] T. Hughes, J.A. Cottrell and Y. Bazilevs. *Isogeometric analysis: CAD, finite elements, NURBS, exact geometry and mesh refinement*. Comput. Methods Appl. Mech. and Engrg., 194:4135-4195, 2005.

[11] A. Herrema, N. Wiese, C. Darling, B. Ganapathysubramanian, A. Krishnamurthy and M. Hsu *A framework for parametric design optimization using isogeometric analysis*. Comput. Methods Appl. Mech. and Engrg., 31:944-965, 2017.

[12] H. Liu, D. Yang, P. Hao and X. Zhu *Isogeometric analysis based topology optimization design with global stress constraint*. Comput. Methods Appl. Mech. and Engrg., 342:625-652, 2018.

[13] Zhen Lei *Isogeometric shell analysis and optimization for structural dynamics*. Ecole Centrale de Lyon, 2015.

[14] E. Wadbro and M. Berggren. *Topology optimization of an acoustic horn*. Comput. Methods Appl. Mech. and Engrg., 196:420-436, 2006.

[15] G. Dodgen and T. Khajah *Shape Optimization of an Acoustic Horn using Differential Evolution and Isogeometric Analysis.* IGA2018, United States Association for Computational Mechanics (USACM), 2018.

[16] B. Engquist and A. Majda. *Absorbing Boundary Conditions for the Numerical Simulation of Waves*. Mathematics of Computation, 31:629-651, 1997.

[17] T. Khajah, X. Antoine and S.P.A Bordas *High Frequency Acoustic Scattering in Isogeometric Analysis*. Waves 2017 (13th International Conference on Mathematical and Numerical Aspects of Wave Propagation), University of Minnesota, Twin Cities Campus, Minneapolis, 2017.

[18] G. Dodgen and T. Khajah *Effectiveness of Tikhonov Smoothing in Isogeometric Shape Optimization of the Horn Speaker*. American Society for Engineering Education Gulf Southwest Conference, University of Texas at Tyler, 2019.

[19] M. Yuan, Z. Cao, J. Luo and X. Chou *Recent Developments of Acoustic Energy Harvesting: A Review*. Micromachines, 10, 2019.

[20] S. Noh, H. Lee and B. Choi *A study on the acoustic energy harvesting with Helmholtz resonator and piezoelectric cantilevers*. Int. J. Precis. Eng. Manuf., 14:1629–1635, 2013.

[21] F.U. Khan *Hybrid acoustic energy harvesting using combined electromagnetic and piezoelectric conversion*. Rev. Sci. Instrum. 87, 2016.

[22] A. Can, J. Lelong and D. Botteldooren *Traffic noise spectrum analysis: Dynamic modeling vs. experimental observations*. Applied Acoustics, 71:764-770, 2010.

[23] H. Noh *Acoustic energy harvesting using piezoelectric generator for railway environmental noise*. Advances in Mechanical Engineering, 10:1-9, 2018.

[24] F. Mir, M. Saadatzi, R. Ahmed and S. Banerjee *Acoustoelastic MetaWall noise barriers for industrial application with simultaneous energy harvesting capability*. Applied Acoustics, 139:282-292, 2018.

[25] Y. Wang, X. Zhu, S. Bano, H. Pan, L. Qi, Z. Zhang and Y. Yuan *A renewable low-frequency acoustic energy harvesting noise barrier for high-speed railways using a Helmholtz resonator and a PVDF film*. Applied Energy, 230:52-61, 2018.

[26] A. Krynkin and O. Umnova *Predictions and measurements of sound transmission through a periodic array of elastic shells in air*. The Journal of the Acoustical Society of America, 128, 2010.

[27] M. Thota and K. Wang *Reconfigurable origami sonic barriers with tunable bandgaps for traffic noise mitigation*. Journal of Applied Physics, 122, 2017.

[28] E. Atroshchenko, C. Anitescu, T. Khajah and T. Rabczuk *Isogeometric Collocation in Acoustics.* IGA2018, United States Association for Computational Mechanics (USACM), 2018.

[29] A. Bayliss, M. Gunzburger and E. Turkel. *Boundary Conditions for the Numerical Solution of Elliptic Equations in Exterior Regions.* SIAM J. Appl. Math, 45:430-451, 1982.

[30] Y. Cheng, C. Zhou, B.G. Yuan, D.J. Wu, Q. Wei and X.J. Liu *Ultra-sparse metasurface for high reflection of low-frequency sound based on artificial Mie resonances*. Nature Materials, 14:1013-1020, 2015.

[31] V. Hadlich and T. Khajah *Design and Optimization of acoustic metamaterials for noise reduction* American Society for Engineering Education Gulf Southwest Conference, 2019.

[32] S.M. Dsouza, T. Khajah, S. Natarajan and S.P.A. Bordas *A Comparative Study of B-Spline- and Lagrange- FEM in solving acoustic scattering problems.* In World Congress in Computational Mechanics (WCCM 2018), 2018.